

Report 4322

ode Arrays

t in

ording

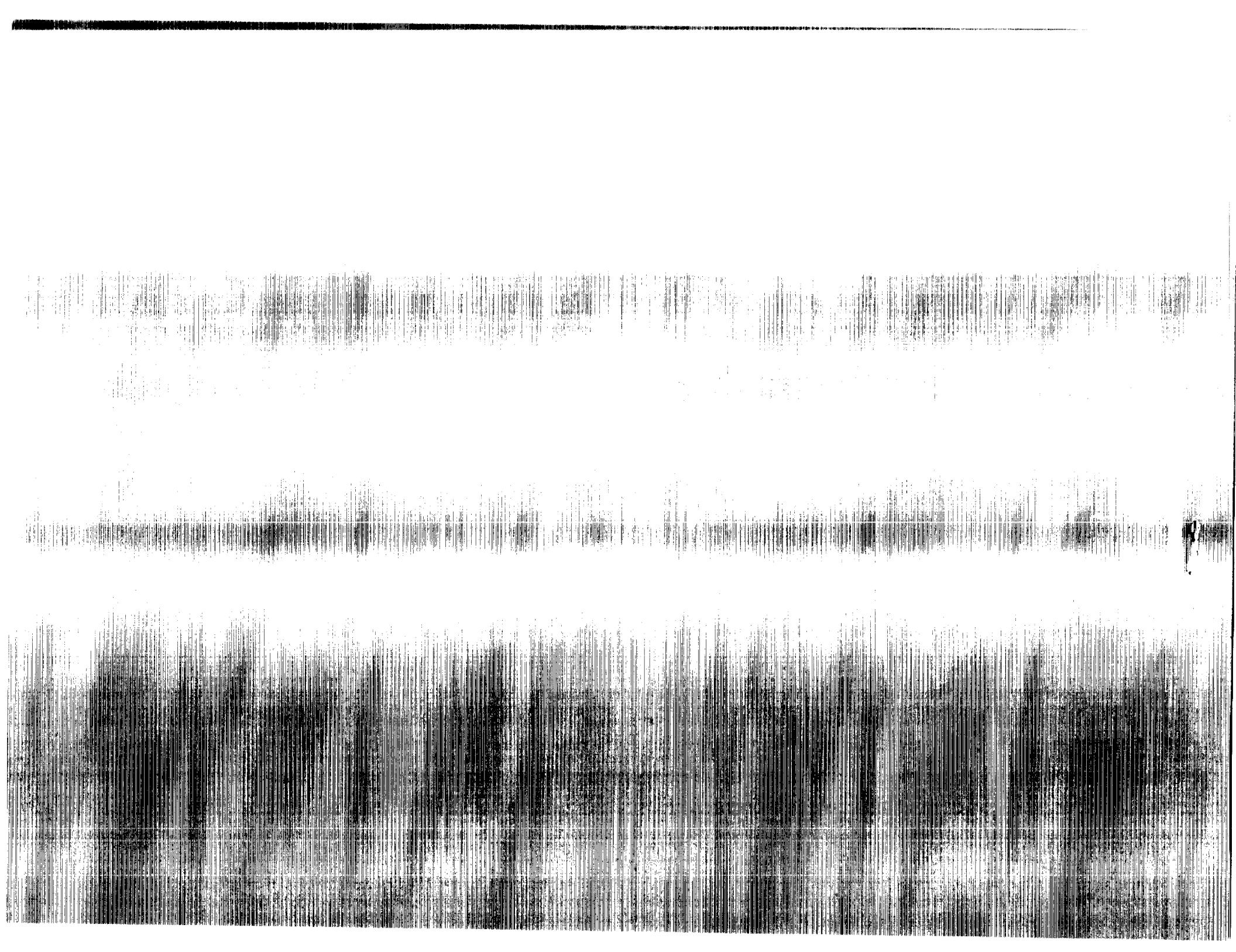
ns

(NASA-CR-4322) LINEAR LASER DIODE ARRAYS
FOR IMPROVEMENT IN OPTICAL DISK RECORDING
FOR SPACE STATIONS Final Report, Mar. 1988 -
Sep. 1989 (David Sarnoff Research Center)
88 p

CSCL 14E H1/36

Unclas

0303920



NASA Contractor Report 4322

Linear Laser Diode Arrays
for Improvement in
Optical Disk Recording
for Space Stations

G. A. Alphonse, D. B. Carlin,
and J. C. Connolly
*David Sarnoff Research Center
Princeton, New Jersey*

Prepared for
Langley Research Center
under Contract NAS1-18226



National Aeronautics and
Space Administration
Office of Management
Scientific and Technical
Information Division

1990

Preface

This report describes work performed from March 28, 1988 to September 1, 1989 at the David Sarnoff Research Center in the Optoelectronics Research Laboratory, M. Ettenberg, Director, on Tasks 4, 6, and 7, under contract No. NASA 1-18226. Tasks 4 and 7 are specifically aimed at the development of ten-element linear diode arrays for optical recording. The goal of Task 6 is the development of high-power AlGaAs channeled substrate planar (CSP) lasers. The work described herein pertains to the design of grating-stabilized CSP structures for use in optical recording applications. D.B. Carlin was the Project Supervisor and was Project Scientist for part of this work. G.A. Alphonse was Project Scientist for the latter part of this work. Other contributors to this research were J.C. Connolly, M.G. Harvey, T.R. Stewart, D.A. Truxal, A.R. Dholakia, F.Z. Hawrylo, S.L. Palfrey, G.C. Taylor, S.N. Subbarao, P.D. Gardner, D.T. Tarangioli, D.J. Holmes, J.P. Bednarz, M. Toda, and J.B. Berkshire.



Table of Contents

Section	Page
	xi
	1
I.	5
II.	5
A.	7
1.	13
2.	14
B.	18
C.	23
III.	23
A.	23
1.	26
2.	28
B.	33
C.	37
D.	41
IV.	41
V.	47
A.	47
B.	49
1.	49
2.	49
3.	50
4.	54
VI.	57
A.	58
1.	58
2.	60
B.	65
C.	66
D.	67
VII.	75
VIII.	77



List of Illustrations

Figure		Page
II-1	Sketch of 10-diode array.....	5
II-2	Array bonded to metallized BeO submount.	6
II-3	Details of CSP array on BeO submount.....	7
II-4	Substrate absorption due to n-confining layer thickness as a function of lateral position for CSP structure of various channel widths.	8
II-5	Calculated P-I characteristics for CSP lasers of various channel widths.....	9
II-6	Second order mode gain and lasing threshold for CSP lasers of various widths.....	10
II-7	Differential quantum efficiency as a function of stripe width for a CSP laser with 6 μm channel width.	11
II-8	Threshold current as a function of diffusion in stripe width for a CSP laser with a 6 μm channel width.....	11
II-9	Differential quantum efficiency as a function of diffusion stripe width for a CSP laser with 8 μm channel width.....	12
II-10	Threshold current as a function of diffusion stripe width for a CSP laser with 8 μm channel width.....	12
II-11	Comparison of (a) CSP and (b) DCC-CSP laser structures.....	13
II-12	Flow chart for characterizing 10-diode arrays.....	15
II-13	P-I and far-field characteristics of 10-diode array from probe tester.	16
II-14	P-I far-field and spectral characteristics of 10-diode array mounted on heatsink before burn-in.....	17
II-15	P-I, far-field and spectral characteristics of 10-diode array after 100-hour burn-in.	18
II-16	Geometry of CSP structure for CSP tolerance analysis and P-I curve bend-over caused by misalignment of zinc diffusion.....	20

List of Illustrations (cont.)

Figure		Page
II-17	Calculated (a) lateral effective index profiles, (b) lateral gain profiles in the active layer, (c) near-field intensity distributions, and (d) far-field intensity patterns for a symmetric CSP-DH structure ($l_1 = l_2 = 2.0 \mu\text{m}$), with a misaligned 4- μm -wide Zn diffusion front for output powers of 0, 5, 10, 15, 20, 25, and 30 mW. The Zn diffusion is misaligned by 0.5 μm	21
III-1	LPE reactor used for growth of CSP lasers.....	23
III-2	Micrograph of CSP growth angle lapped at 1° angle showing (a) terraced active layer and (b) non-terraced active layer.....	26
III-3	MOCVD reactor.	27
III-4	Front-end CSP processing flow chart.	29
III-5	Front-end CSP fabrication step.....	30
III-6	Back-end processing steps for CSP fabrication.	31
III-7	Cleaving, facet coating, and chipping.	33
III-8	Heat flow model of Nakwaski. (1) Directly through stripe contact. (2) Flowing far from source to reach heat sink through oxide layer. (3) Flowing through regions far from heatsink, but reaching heatsink through stripe. "The oxide layer, ... effectively confines heat spreading in the lateral direction."	35
III-9	Ishikawa's cause and effect diagram for diode reliability.....	36
III-10	Fixture for machine-assisted bonding of diode arrays.....	38
III-11	(a) Array containing seven lasers bonded by fluxless machine-assisted method using gold-tin bond. (b) Front facet of array containing seven lasers bonded by fluxless machine-assisted method using gold-tin bond.....	39
III-12	P-I characteristics of seven-laser array bonded by fluxless machine-assisted methods.	40
IV-1	Monolithic double heterojunction I-CSP array. The QW structure is obtained by substituting the QW and confining layers for the active layer.	41

List of Illustrations (cont.)

Figure		Page
IV-2	Process steps for I-CSP arrays.....	43
IV-3	A ridge QW laser diode array.....	44
IV-4	Far-field pattern of ridge QW laser array.....	45
V-1	Configuration of bismuth-substituted gadolinium iron garnet Faraday rotator as built-in isolator window for laser diode array.....	50
V-2	Laser-superluminescent diode (SLD) array insensitive to feedback. When a positive voltage is applied to the large electrode at the left, the array functions as an array of high-power individually addressable laser diode array. When it is disconnected or reverse biased, the structure functions as an SLD array whose output is unaffected by feedback.....	51
V-3	Broadband spectrum of superluminescent diode.....	52
V-4	Relative noise $20 \lg(d/I)$ of SLD (open circle) and of a laser from the same wafer (black circles). Also shown is the P-I of a laser (solid line) and of SLD (dashed line).....	52
V-5	Configuration using separate sources for write-erase and for read. The optics for write-erase sources contain a polarizing beam splitter and a quarter-wave plate to prevent feedback. The read sources are diodes, such as DFB or DBR lasers, SLDs, or lasers with built-in isolators. Readout detectors are not shown.....	53
V-6	Two-dimensional array that can be used either as a direct-read-after-write or as source with built-in redundancy.....	54
V-7	Spectrum of Fabry-Perot laser near threshold.....	55
VI-1	(a) Structure of DFB laser. The grating is along the active region. (b) Structure of DBR laser. The gratings are placed in passive regions at the ends of the active region. They serve mainly as wavelength selective reflectors.....	57
VI-2a	Ideal DFB has two modes with lowest threshold, identified by arrows.....	62

List of Illustrations (cont.)

Figure		Page
VI-2b	Shifting gain curve to select one mode.....	62
VI-2c	Use of radiation loss to select single mode.....	63
VI-2d	Creating low threshold "gap mode" at the Bragg wavelength.....	63
VI-3	Relation of threshold gain to coupling coefficient for DFB lasers.....	64
VI-4	Plot of coupling coefficient for triangular grating in DFB lasers.....	65
VI-5	A "divide-by-two" method to produce grating with period in the 1000Å range.	69
VI-6	Alternative method to produce short period gratings (details in text).	70
VI-7	Third method for producing short period gratings.....	70
VI-8	Grating shape categorized as good and poor for second order DFB laser.	72

EXECUTIVE SUMMARY

This report describes the work on a program aimed at the development of monolithic arrays of individually addressable AlGaAs laser diode arrays for use as the source of light in high data rate multichannel optical data storage systems. Improvements to the design of CSP (channel substrate planar) arrays and a better understanding of the critical device and processing parameters, have led to the fabrication, testing and delivery of ten-diode arrays having output power exceeding 30 mW cw, linear light vs current characteristics and single longitudinal mode spectral characteristics. The limitations of CSP structures are examined, and the inverse CSP (ICSP) structure, grown by metalorganic chemical vapor deposition technique (MOCVD), is presented as one whose fabrication is less critically dependent on device parameters than the CSP. Preliminary results on quantum well ICSP arrays indicate that this structure also lead to threshold currents of 12 to 15 mA, as compared to 40-60 mA for CSPs. The salient features of this work include:

- The complete evaluation and understanding of the CSP approach
- Improvement of processing techniques leading to the fabrication of deliverable arrays
- The demonstration of new arrays grown by MOCVD having threshold current less than one-half the threshold current of LPE arrays
- The demonstration of machine-assisted bonding technique suitable for space application

We explore, at length, the impact of systems response and requirements, in particular the effect of feedback, on laser design. We examine several alternative techniques both in systems design and laser structure to reduce feedback or minimize its effect on systems performance. They include the use of high frequency modulation, optical isolators, dual source techniques, and wavelength-stabilized sources. From the viewpoint of laser design, we show that structures having frequency selective feedback, such as DFB and DBR structures, provide the desired longitudinal modes stability. Finally we present an analysis DFB and DBR lasers and fabrication considerations leading to the choice of DFB lasers as suitable for magneto-optic recording systems.

Section I

INTRODUCTION

Much effort has gone into the development of optical data storage.[1-6] All the approaches considered over the past twenty years (page oriented holography, volume holography, optical disk, optical tape, etc) entail some trade-off between storage density, random access, capacity, size, speed, access time, and rewritability. Only the erasable optical disk offers a balanced trade-off between these parameters.[7]

One of the most powerful advantages of optical disk is the fact that, despite the small size of the optical head, the light beams from several lasers can be designed to fit within its aperture for writing, reading, and erasing. This implies that an appropriately designed array of light sources can be used to achieve parallel or multichannel operation and thus increase the data rate by a factor equal to the number of read-write source elements. Multichannel recording is the only demonstrated technique for achieving data rates of 200 or more Mb/s in optical data storage systems.[8]

There has been a steady evolution in the development of optical disk systems. The early emergence of write-once-read-many times, also called WORM, systems has spurred the development of compact drives, many of which are already on the market. This has paved the way for efforts on read-write-erase systems, which required considerable work, mainly in media development. The two main media candidates have been the tellurium-based phase change media and magneto-optic (MO) media.[9] Due to its potential for high rewritability without fatigue, MO is now emerging as the primary medium for erasable or rewritable optical disks.[10]

There are several constraints imposed on a laser diode array for multichannel recording. Some are physical, and some relate to performance. From the physical viewpoint, the laser elements must have a close enough spacing between elements in order for all the beams to be handled by only one optical system. They must be individually addressable in order for the channels to be independent, they must be aligned with respect to one another, and the number of elements in a package must make sense from the viewpoint of data manipulation, i.e., one half byte or one byte in a package, plus extras for tracking.

Those physical constraints have led us to design monolithic arrays of individually addressable laser diodes with close spacing between elements.

The constraints on performance impose requirements on the wavelength, output power, and relative intensity noise. Short wavelength diodes are desired for high packing density. The power and noise requirements are of particular importance to MO systems because the recording sensitivity is somewhat lower (higher power requirement) for MO than for other media. Also, the sensitivity to relative intensity noise of laser diode sources is more critical in these than in other systems. Aluminum gallium arsenide diodes operating at 830 nm wavelength are compact, have high electrical to optical power conversion efficiency, are easy to modulate, and have potentially long life. Furthermore, channel substrate planar (CSP) diodes have been shown to emit high output power (greater than 30 mW) in a single longitudinal mode. For this reason, the CSP has been chosen as the baseline structure for our arrays.

We have developed two types of CSP structures. The first one is the standard type with a V-groove channel etched in the substrate, and with the functional layers (n-clad, active p-clad, and cap) grown over the groove. The active stripe is defined by zinc diffusion through an oxide mask over the channel. We have discovered that optimization of power conversion efficiency requires the zinc diffusion stripe be narrower than the channel, but that device performance is severely sensitive to stripe misalignment. Since the CSP structure is grown by liquid phase epitaxy (LPE), which is subject to growth non-uniformity, device yield tends to be low. An alternate structure is the inverse CSP (I-CSP), in which the channel is created in the p-clad by etching away the regions on the sides of the lasing stripe and regrowing a blocking layer in its place. The structure is self-aligned and should be free from the misalignment problem encountered in the ordinary CSP. Furthermore, it is grown by metalorganic chemical vapor deposition (MOCVD), which is very uniform and capable of producing devices with high yield.

As mentioned earlier, MO disk systems require lasers to have low relative intensity noise (RIN) in the readout mode. The signal-to-noise ratio (SNR) in MO readout is inherently low due to the low level of the output signal. MO readout is obtained through the Kerr effect which transforms a linearly polarized light into an elliptically polarized reflected light, and the output signal is the rotated component of the light. Since the rotation angle is small (less than one degree), the field component corresponding to the readout signal is very small, resulting

in an output signal with low SNR. Part of the reflected light is fed back to the laser and causes the laser wavelength to hop from one longitudinal Fabry-Perot mode to another, with generation of noise in the MHz range, i.e., in the signal base band. This phenomenon is most pronounced when the laser power is around the readout level (a few milliwatts) and when the feedback into the laser is in the 1% to 10% range. The effects of feedback into CSP lasers on systems performance are well known. We have assessed this problem in the course of this work and have examined several solutions. They include the use of isolators, wavelength stabilized lasers, laser modulation, separate write and read sources, as well as the use of broadband sources for readout.

This report covers our work on CSP and I-CSP arrays and assesses techniques to enhance systems operation. Such techniques include the use of separate sources for reading and writing-erasing, the use of wavelength-stabilized sources. This report also includes a description of our work toward the development of techniques for mounting arrays for operation in space.

Section II

CSP LASER ARRAYS

A. BASELINE STRUCTURE AND GROWTH TECHNIQUE

The design of an individually addressable array involves not only the epitaxial structure that makes up the laser elements, but also the configuration required to make the array functional. The design must provide not only for thermal, electrical and optical isolation between laser elements, but also low thermal resistance to a heatsink and matching thermal expansion among the various parts of the overall structure. A sketch of our design that best fits these requirements is shown in Fig. II-1.

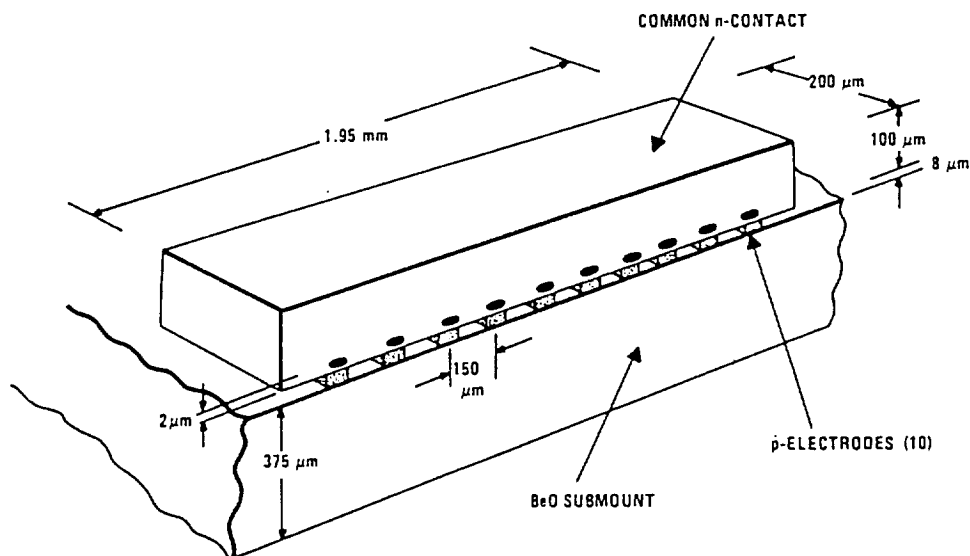


Figure II-1. Sketch of 10-diode array.

The array consists of a GaAs bar of thickness $100\ \mu\text{m}$, active length $200\ \mu\text{m}$, and total width $1.95\ \text{mm}$, containing 10 AlGaAs CSP diodes emitting light at $830\ \text{nm}$, with $150\ \mu\text{m}$ center-to-center spacing consisting of $100\ \mu\text{m}$ metallization and $50\ \mu\text{m}$ electrical isolation. The bar is mounted junction down on a BeO submount whose surface contains an electrode pattern that matches the p-electrode spacing on the GaAs, with a suitable fan-out for electrical connection, a top view of which is shown in Fig. II-2.

ORIGINAL PAGE
BLACK AND WHITE PHOTOGRAPH

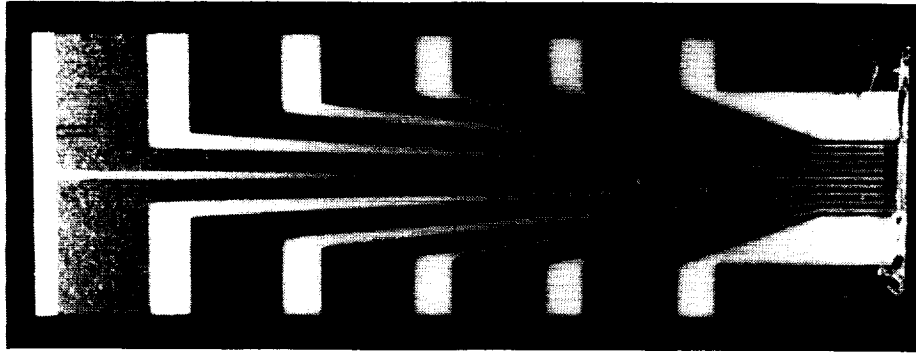


Figure II-2. Array bonded to metallized BeO submount.

BeO is used as a submount because, while being an electrical insulator, it also has relatively high thermal conductivity and a coefficient of thermal expansion that matches that of GaAs. The front facet of the array must be positioned to within only a few microns of the submount edge, to avoid obscuring the highly divergent output beam. Also, the array must be positioned laterally to a tolerance of $\pm 50 \mu\text{m}$ because of the narrow electrical isolation channels in the chip and the small separation of the electrode fingers. The n-side of the array is electrically connected to each of two submount grounding pads using large cross-section gold ribbon to carry the combined currents necessary to operate all diodes simultaneously. The submount is attached to a thermoelectrically cooled copper heatsink maintained at $\approx 23^\circ\text{C}$ to keep the laser threshold current (and light output) constant and to reduce thermal degradation of the laser (life decreases exponentially with increasing temperature).

A detailed view of the CSP structure on the BeO submount is shown in Fig. II-3 (This view is upside down compared to the view of Fig. II-2). In addition to the baseline CSP, this figure shows a $50\text{-}\mu\text{m}$ -wide groove that has been ion-milled out of the p-side of the bar and cutting through all the epitaxially grown layers. As pointed out earlier, this groove is designed to provide not only electrical, but also optical and partial thermal isolation between the laser elements.

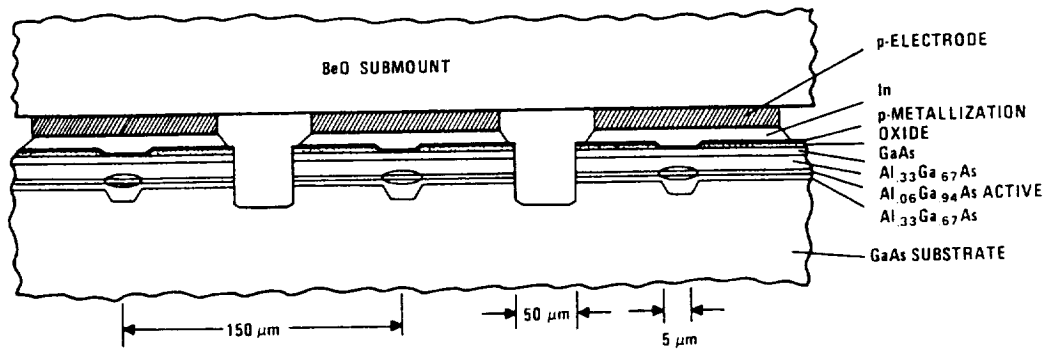


Figure II-3. Details of CSP array on BeO submount.

1. Baseline CSP Design

The baseline CSP structure is also shown in Fig. II-3, with compositions and thicknesses listed on the right side of the sketch. Light is generated in a thin ($\approx 1000\text{-\AA}$ -thick) active layer of undoped $\text{Al}_{.06}\text{Ga}_{.94}\text{As}$ sandwiched between cladding layers of p-doped and n-doped AlGaAs (top and bottom of the figure, respectively) of higher aluminum concentration. This stack of layers forms a real index guide that confines the laser light in the transverse direction (perpendicular of the heterojunction plane). The injection current is confined both by a narrow contact stripe in the p-side metallization, defined by a SiO_2 insulation film deposited on the GaAs cap layer, and by the diffusion of a zinc finger partially through the p-cladding layer. The injection current would itself confine the lateral spatial mode (parallel to the junctions) by affecting the gain distribution, but such a gain-guided laser structure would emit an astigmatic beam of light. The lateral spatial mode is also well-confined by the shoulders of the channel. The laser light has a higher energy than the bandgap of the n-GaAs substrate material and is, therefore, heavily absorbed outside the channel region. In addition, the indices of refraction of the layers support radiation modes into the substrate, which also increase the loss outside of the channel.

The design of high power single mode CSP lasers depends critically upon three parameters: the thickness of the n-confinement layer, the width of the V-groove channel, and the width of the zinc diffusion stripe. We found that the optimum design is one in which the thickness of the n-confinement layer is $0.3\ \mu\text{m}$ to $0.4\ \mu\text{m}$ for proper lateral mode control. The optimum channel width is $6\ \mu\text{m}$ to $8\ \mu\text{m}$ to minimize losses and prevent the excitation of higher order modes.

The zinc diffusion stripe width is less than the channel width, i.e., $5\ \mu\text{m}$ or less in order to minimize threshold current and maximize differential quantum efficiency (DQE). These parameters were obtained from modeling studies, whose results are shown in Figs. II-4, II-5, and II-6. Figure II-4 is a plot of substrate absorption due to the thickness of the n-confining layer as a function of lateral position for channel width ranging from $4\ \mu\text{m}$ to $10\ \mu\text{m}$, for a zinc diffusion width of $6\ \mu\text{m}$. The insert is a description of the layer structure. Figure II-5 shows the calculated P-I characteristics under these same conditions, and Fig. II-6 represents the gain of the second order mode as a function of current, also with channel width as a parameter. In particular, it indicates the required gain coefficient for lasing in the second order mode. These figures indicate that a wide channel is preferable in order to reduce losses and increase DQE, but that it should be limited to between $6\ \mu\text{m}$ and $8\ \mu\text{m}$ to prevent lasing in higher order modes at the normal operating current of CSP lasers ($100\ \text{mA}$ to $175\ \text{mA}$).

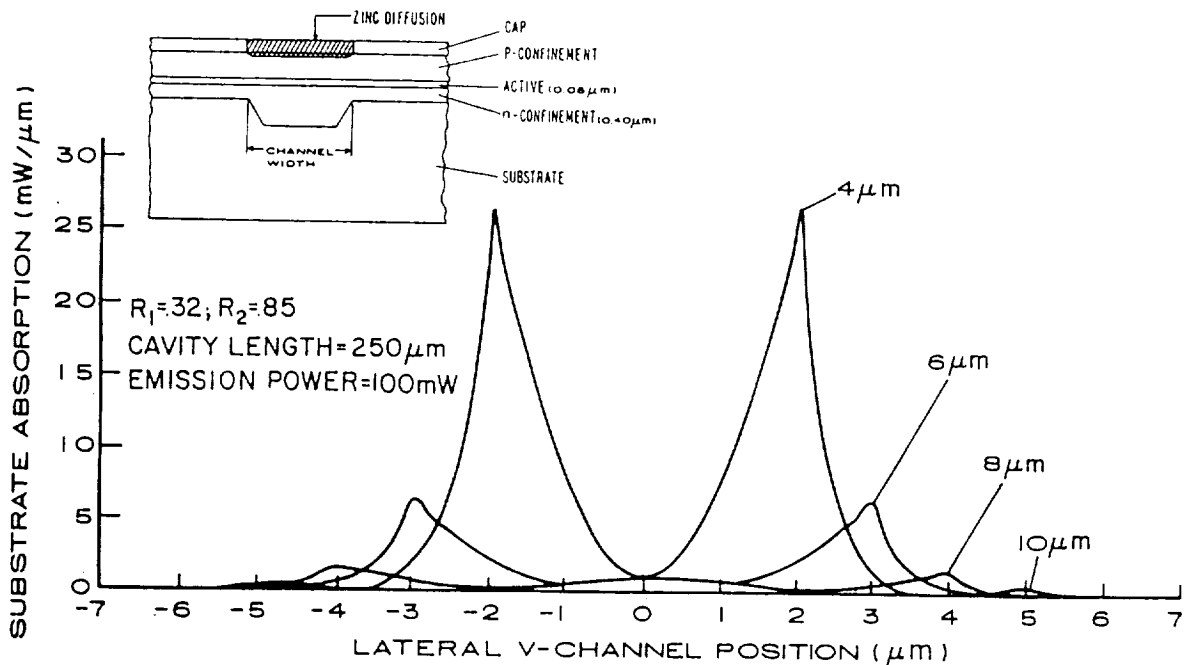


Figure II-4. Substrate absorption due to n-confining layer thickness as a function of lateral position for CSP structure of various channel widths.

ORIGINAL PAGE IS
OF POOR QUALITY

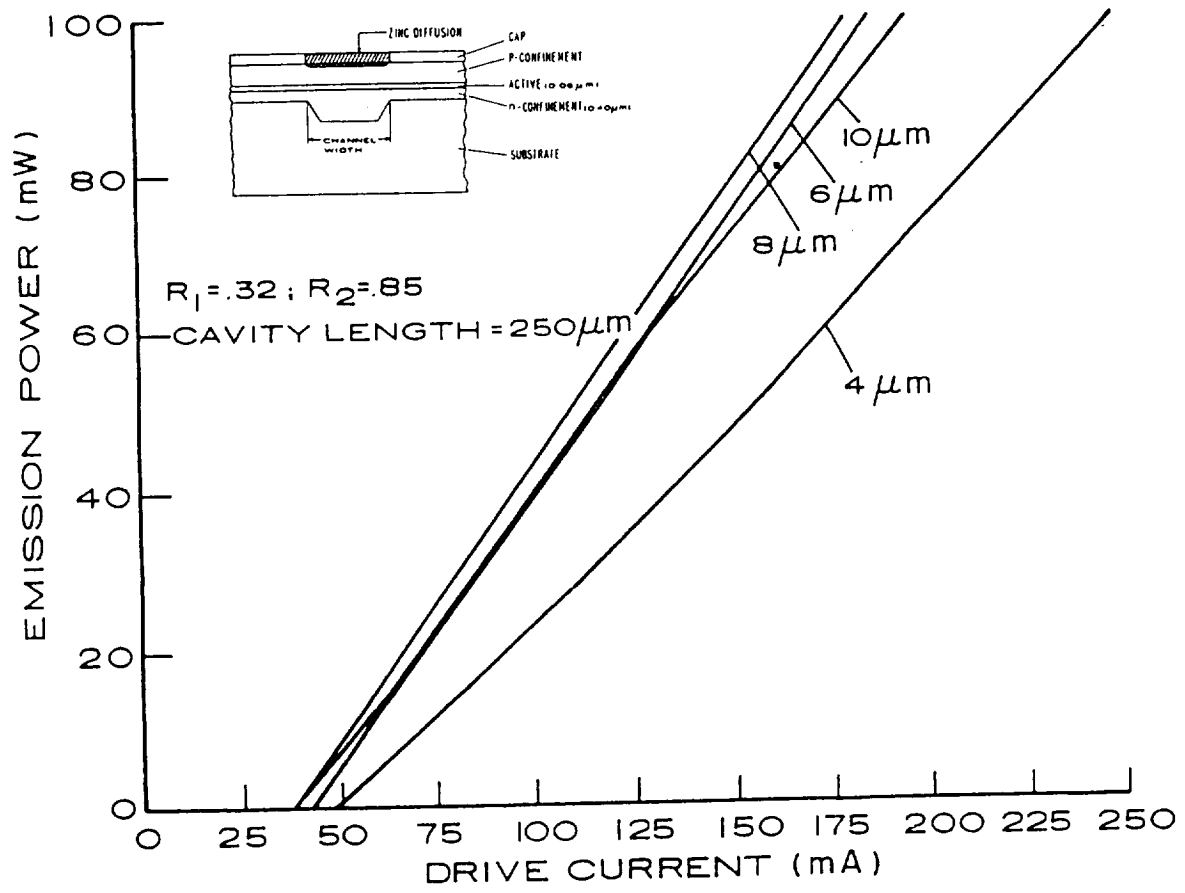


Figure II-5. Calculated P-I characteristics for CSP lasers of various channel widths.

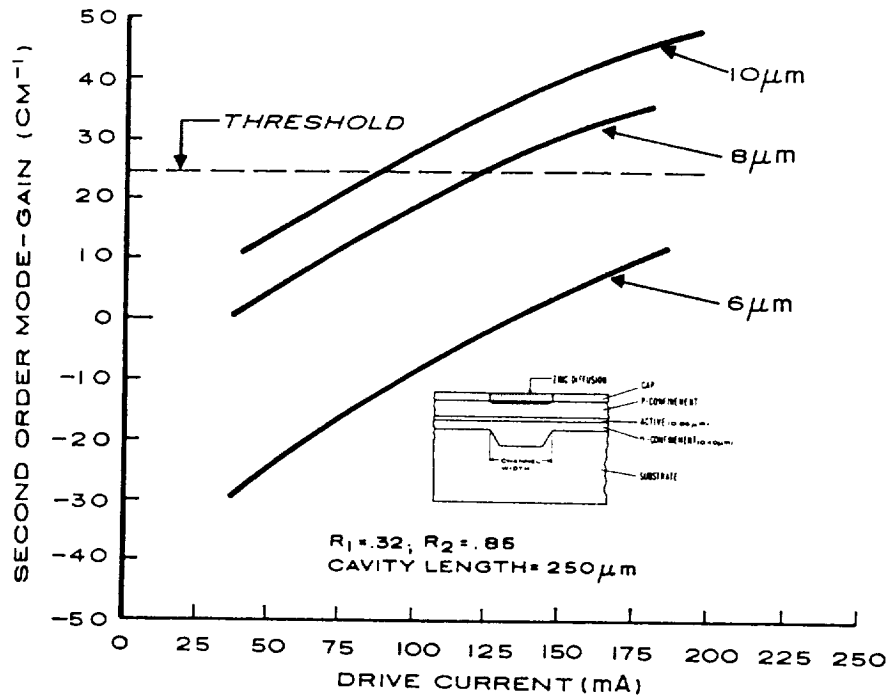


Figure II-6. Second order mode gain and lasing threshold for CSP lasers of various widths.

Having determined the optimum channel width, we optimized the zinc diffusion stripe width. This was done by examining the threshold current density and DQE as a function of stripe width for a laser having 6-μm- and 8-μm-wide channels. The results are plotted in Figs. II-7, II-8, II-9, and II-10. For the 6-μm channel, the optimum stripe width has a broad minimum around 3 μm. For the 8 μm channel, the optimum stripe width is about 5 μm. Since it is easier to make contact to a wide stripe than to a narrow stripe, we chose a compromise value of 4 μm to 3.5 μm for the stripe width. Thus, for the reasons discussed, our baseline CSP design consists of 6 μm-wide channel with 4 μm zinc diffusion stripe. If desired, the latter can be increased to 4.5 μm or 5 μm by over-etching the SiO₂ zinc diffusion mask.

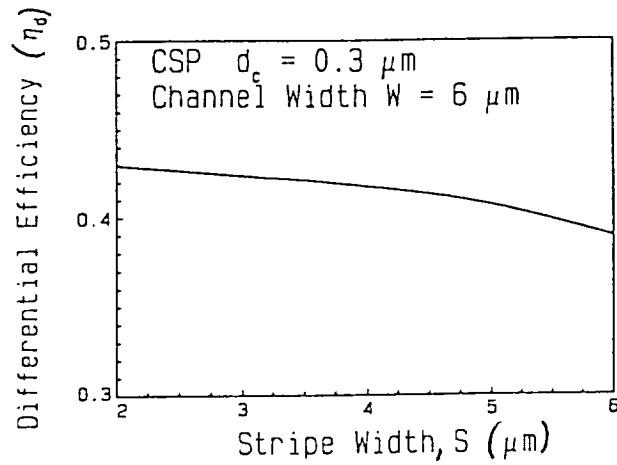


Figure II-7. Differential quantum efficiency as a function of stripe width for a CSP laser with $6 \mu\text{m}$ channel width.

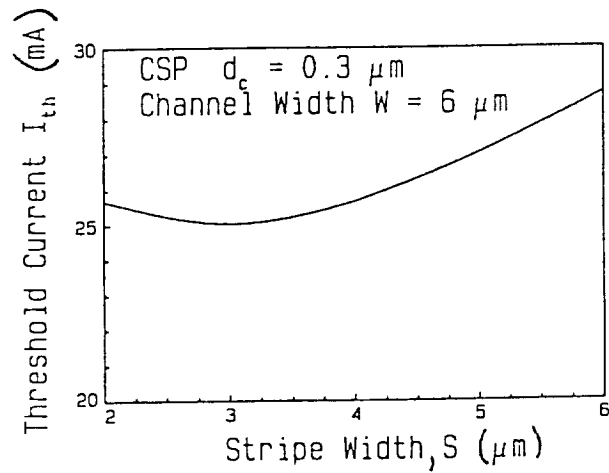


Figure II-8. Threshold current as a function of diffusion in stripe width for a CSP laser with a $6 \mu\text{m}$ channel width.

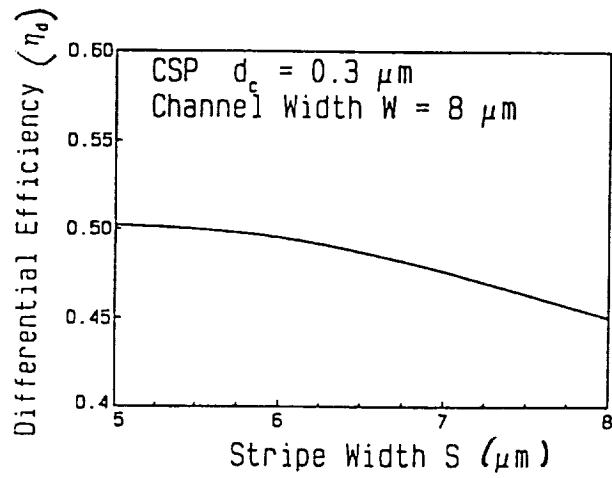


Figure II-9. Differential quantum efficiency as a function of diffusion stripe width for a CSP laser with $8 \mu\text{m}$ channel width.

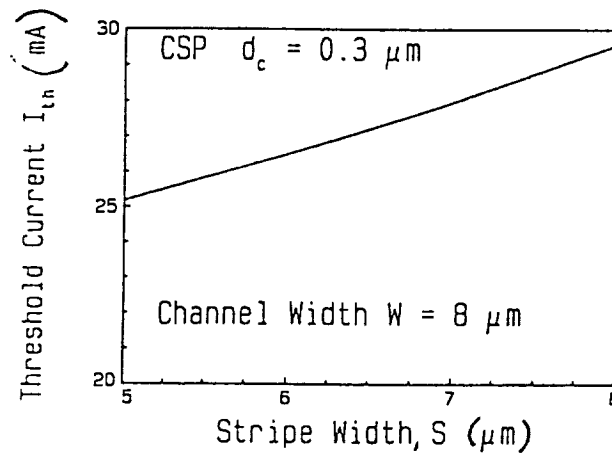


Figure II-10. Threshold current as a function of diffusion stripe width for a CSP laser with $8 \mu\text{m}$ channel width.

2. DCC CSP

The creation of the p-contact by zinc diffusion through the n-clad layer is the chief mechanism for controlling current spreading in the structure. However, zinc can also diffuse into the cap through pinholes in the SiO₂ mask, resulting in shunting currents at various locations. The shunting currents can be prevented, and more efficient devices can be created, by growing a current blocking layer on the n-side of the structure. Such a structure is called the double current confinement-channel substrate planar (DCC-CSP). Figure II-11a is a sketch of the CSP described so far, and Fig. II-11b is the DCC-CSP. The current blocking layer is p-type GaAs grown on the substrate, and it is represented by the shaded area around the groove. The channel is etched out of the blocking layers, then the ordinary CSP is grown afterwards. The only difference between the CSP and the DCC-CSP is in the fact that the channel is etched directly in the substrate in the CSP, whereas it is etched through the blocking layer in the DCC-CSP. The result is that the whole wafer acts as a reversed biased diode everywhere except along the zinc diffusion stripe where current flow is desired.

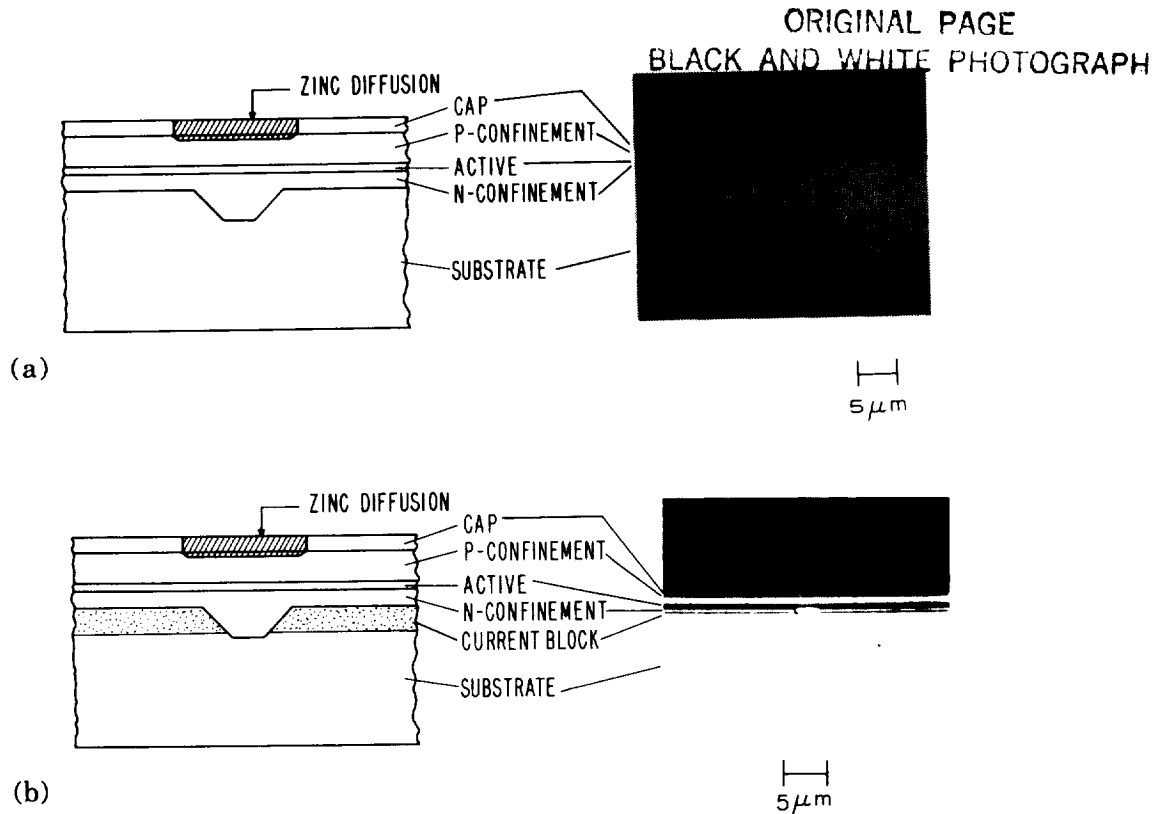


Figure II-11. Comparison of (a) CSP and (b) DCC-CSP laser structures.

B. RESULTS

A total of 38 CSP wafers were grown by LPE, processed, and tested. The fabrication procedure is described in a later section. At this point, the yield for bars with 10 "good" diodes is low. We have identified several of the reasons for the low yield and we have taken corrective action toward them. A "good" array is one having nine or ten contiguous diodes on a single chip, with threshold within about 10 mA of each other, with no kinks and significant rollover in the P-I characteristics, more than 30 mW cw, fairly well superimposed far-fields, and no visible instability in the position of the near-field spot during probe testing.

While several wafers yielded promising results, only one run, wafer TJ 300 had a relatively good yield. It allowed us to attain several 10-diode arrays, which could be bonded on BeO, burned-in for 100 hours, and put on life testing. The characterization procedure is shown in the flow chart of Fig. II-12. Results for one of two 10-diode arrays delivered to NASA are shown in Figs. II-13, II-14, and II-15.

Figure II-13 shows the P-I and far-field characteristics from the probe testing step for sample AT-214. In the probe tester, the array is not permanently bonded, so it is tested with low duty-cycle current pulses. The purpose of probe testing is to weed out arrays that have less than nine acceptable contiguous elements having comparable characteristics. Sample AT-214 was considered acceptable at probe testing.

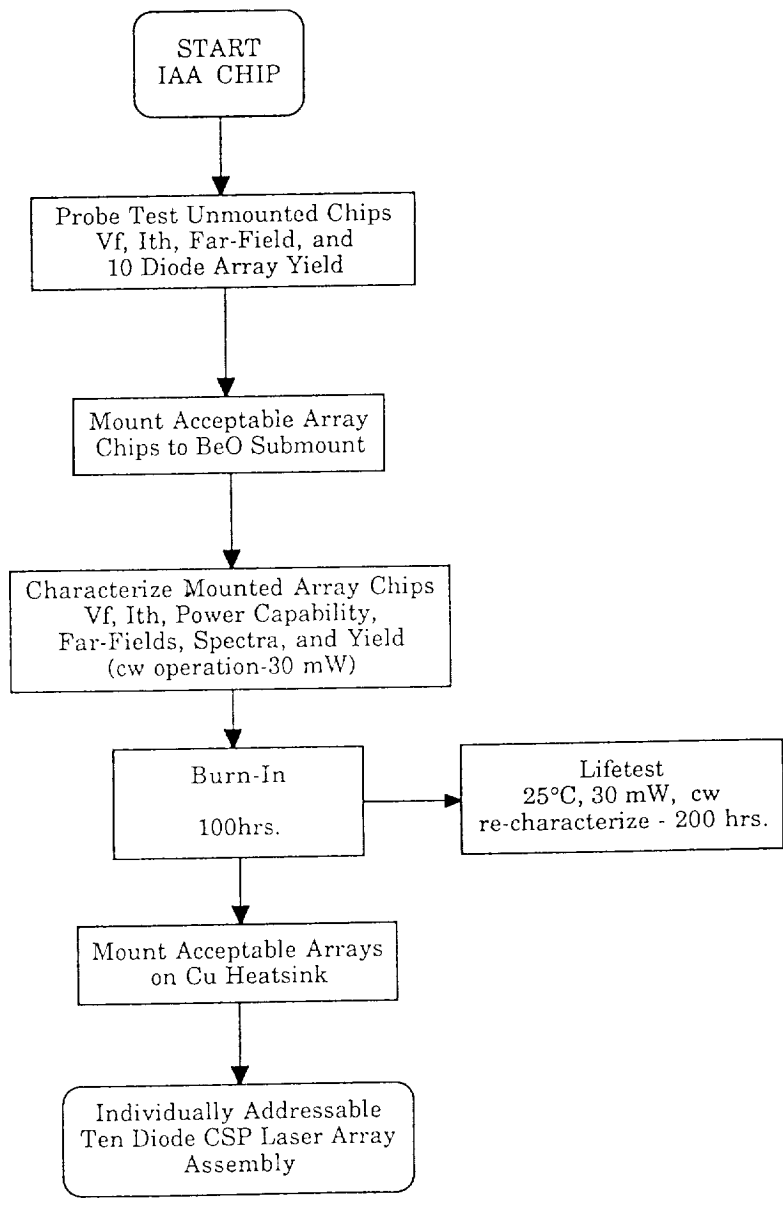


Figure II-12. Flow chart for characterizing 10-diode arrays.

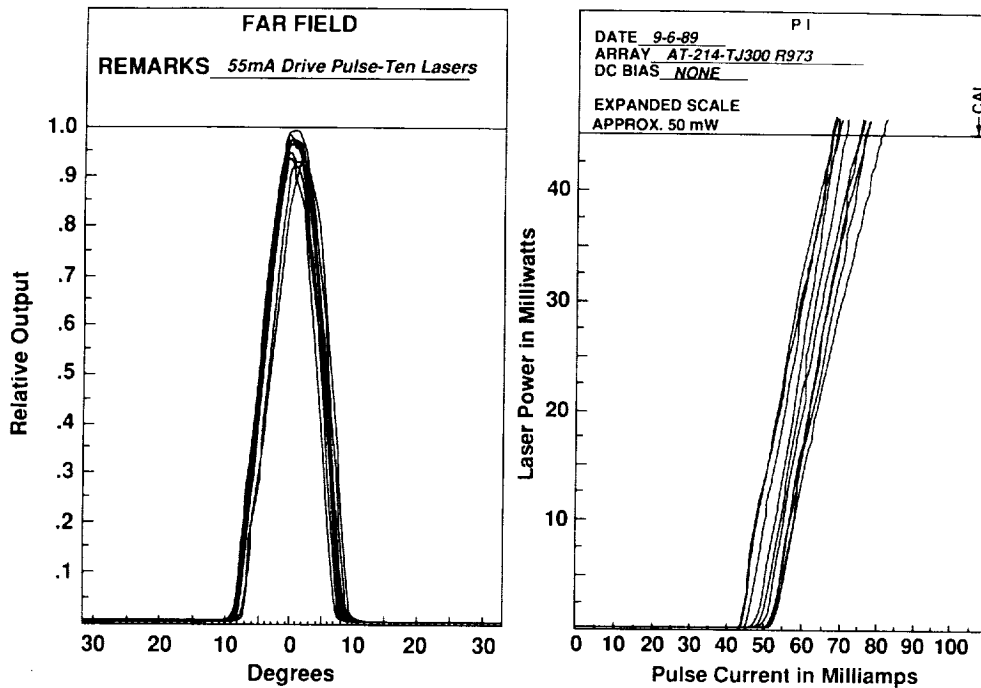


Figure II-13. P-I and far-field characteristics of 10-diode array from probe tester.

Following acceptance at probe testing, the array is hand mounted on the BeO submount using indium solder with flux. A fluxless gold-tin machine-assisted process has been developed for future use, and it is described in another section of this report. The array-on-BeO is then bonded to a gold-plated copper heatsink. Until recently, silver epoxy had been used for this bond. We have developed an indium-tin process to eliminate the silver epoxy, and it is anticipated that future devices will be bonded to the heatsink by this process. The array in the heatsink package is then tested for cw operation, and the P-I characteristics to 30 mW cw, spectra and far-field at 30 mW are measured. The data for array AT-214 are shown in Fig. II-14 and it is considered as the reference point at zero hour burn-in. We observe that the P-I and far-field data for the mounted device are in agreement with the probe testing results. Note that the cw threshold appears higher than in probe testing by about 20 mA. The current shown in probe testing is the applied pulsed current. The legend in Fig. II-13 also shows that a 20 mA bias was applied to the diode (as a forward bias for electrical matching purposes), thus, the threshold data is consistent. Except for diode No. 8, which has a small sidelobe, all the lasers are single spectral mode. The wavelengths spread is only 2.5 nm around 815.45 nm under 30 mW cw operating condition, i.e., the average

wavelength of the array is $815.45 \text{ nm} \pm 1.25 \text{ nm}$. The far-field full widths at half power are all about $10^\circ \times 26^\circ$ (only the lateral far-field is shown), and the slope efficiencies are 0.48 mW/mA .

The same data after 100 h burn-in are shown in Fig. II-15. The results follow closely those obtained prior to burning-in, except for a 5% drop in slope efficiency, the appearance of a spectral sidelobe in diode No. 2, a slight shift toward longer wavelength and a slight increase in the wavelength spread ($816.58 \text{ nm} \pm 1.5 \text{ nm}$).

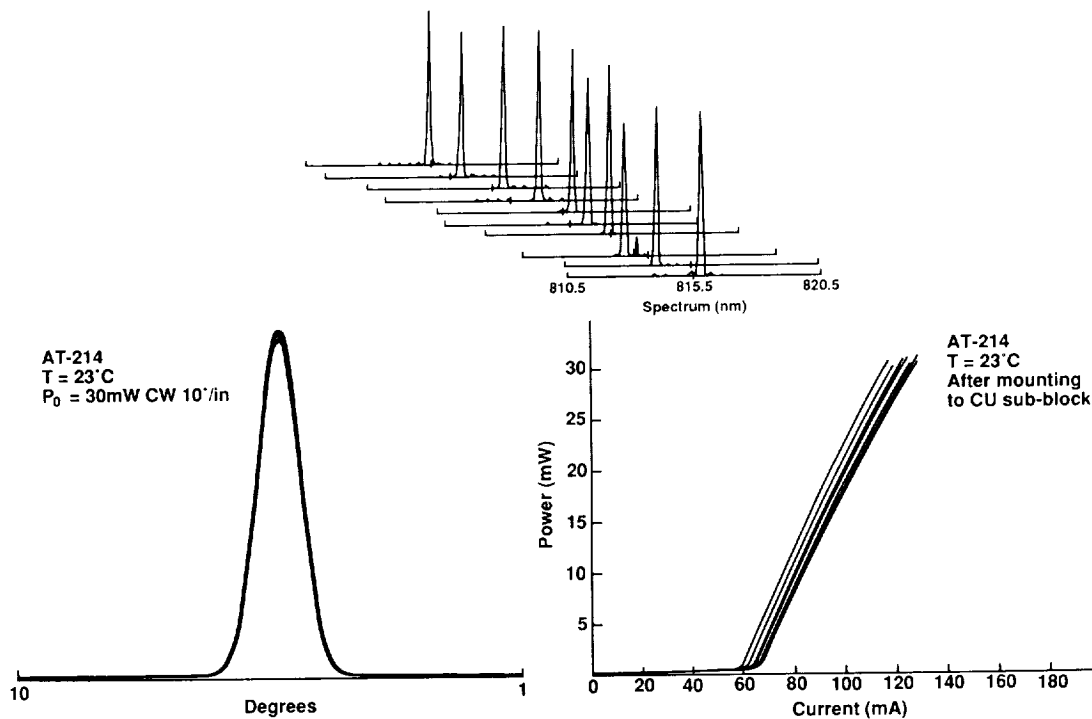


Figure II-14. P-I far-field and spectral characteristics of 10-diode array mounted on heatsink before burn-in.

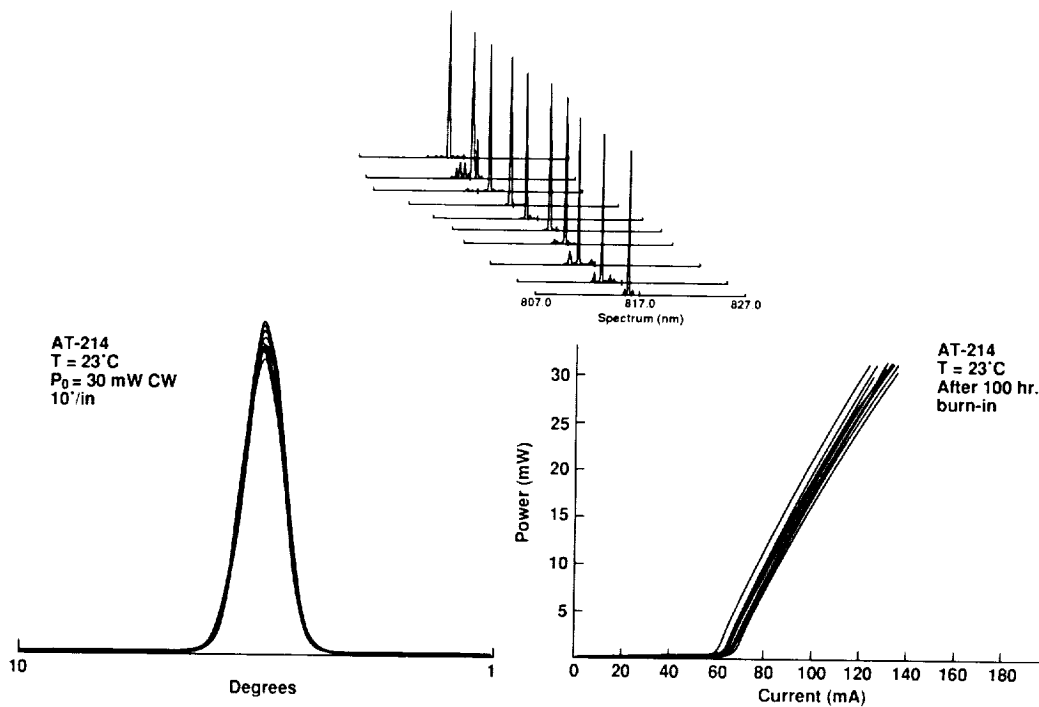


Figure II-15. P-I, far-field and spectral characteristics of 10-diode array after 100-hour burn-in.

C. ISSUES CONCERNING CSP DESIGN AND FABRICATION

As mentioned earlier, the yield of nine and ten-element CSP arrays has been low. Several problems were discovered during probe testing. They were: kinks in the P-I characteristics, roll over at power levels below the rated 30 mW power (saturation at low power level), incomplete arrays, instability of the near-field, variations in threshold current from diode to diode, etc. Some of those problems were related to substrate orientation, others to the CSP growth, others to the CSP design itself, and others to fabrication.

The most obvious problems were those related to fabrication. It was observed that often the end diodes, i.e., diode No. 1, 2, or 9, 10 were physically damaged. This problem was traced to the scribe used to cleave the bars. A new scribe was used that marked the wafer in the areas far from the end elements, and that particular problem was eliminated. This resulted in a significant increase of 10 contiguous elements yield, at least in probe-testing.

The problem with kinks in the P-I curves had two probable causes. One was the fact that the GaAs substrates supplied by the vendor were not oriented

with sufficient accuracy. The substrates, purchased in lots of 50 units, are cut from a single boule, and their orientation must be maintained to less than $.05^\circ$ with respect to the (100) plane during cutting and polishing. If this tolerance is not maintained, terraces on the surface cause variations in growth that result in kinks in device P-I characteristics. We found that x-ray techniques were not sensitive enough to detect misorientation variations. The most practical way to qualify lots was to grow devices on selected wafers and observe the absence or presence of kinks. We adopted a procedure of LPE growth of CSP structures on three substrates from a lot (top, middle, bottom). The lot was accepted if devices showed few or no kinks, and rejected if kinks were prevalent.

The problems of low power saturation (rollover), and near-field instability may be attributable to the lack of fabrication tolerance allowed by the CSP design itself. The optimum CSP design, with a zinc diffusion stripe narrower than the channel, is very intolerant to stripe misalignment and to channel asymmetry (which can occur during etching). This problem has been studied in detail [11-17] and the results are summarized here. For the purpose of the analysis, the channel, active layer, and cladding layers are pictured as in Fig. II-16. The channel width W is $l_1 + l_2$. The stripe width is $4 \mu\text{m}$ and the cavity length is $250 \mu\text{m}$. We only present results of calculations for the case of misalignment. We clearly see the rollover of the P-I curve, and it is attributed to power saturation due to heating resulting from optical absorption along the edge of the channel.

Heating, hence rollover, can sometime be attributed to high thermal resistance of the bond between the p-contact and the BeO submount, and between the latter and the heatsink. Currently, the array is bonded to the BeO by means of indium solder and a flux is used to remove surface oxides. Incomplete removal of the flux and the formation of intermetallic compounds can be causes for high thermal resistance. In the long range, a fluxless method must be used to bond the array to the submount. Such a method has been developed at Sarnoff, and it will be discussed in a different part of this report.

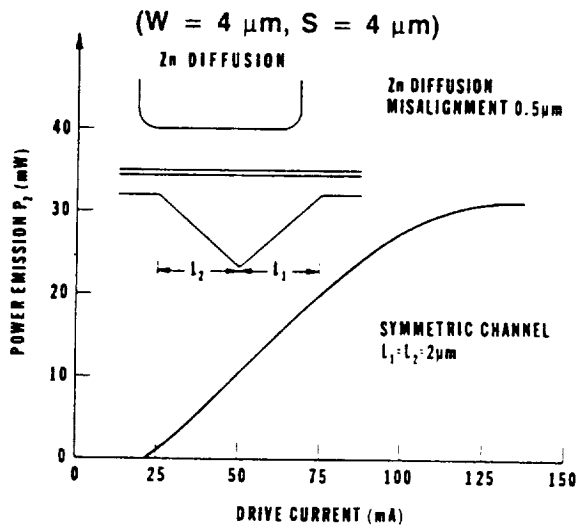


Figure II-16. Geometry of CSP structure for CSP tolerance analysis and P-I curve bend-over caused by misalignment of zinc diffusion.

The interplay between effective index, gain profile, and near- and far-field distribution is shown in Fig. II-17 for a 0.5 μm misalignment in the negative direction. There is an increasing effective index asymmetry with increasing power, which shifts the gain away from the center of the channel. As a result, the power saturates since increased drive current reduces coupling of the spontaneous emission with cavity mode. Also, the large gain region is over the edge of the channel where substrate absorption is high. This causes heating, which may also be responsible for the P-I effects shown in Fig. II-16.

These results have been observed experimentally in the course of our program. The effect of misalignment can be minimized by making the zinc diffusion region wider than the channel. However, this will result in a decrease in efficiency, as described earlier. The best solution is to use a self-aligned structure, rather than CSP. Toward that goal, we started the development of the inverse channel substrate planar (I-CSP) laser structure, and it is described in section IV.

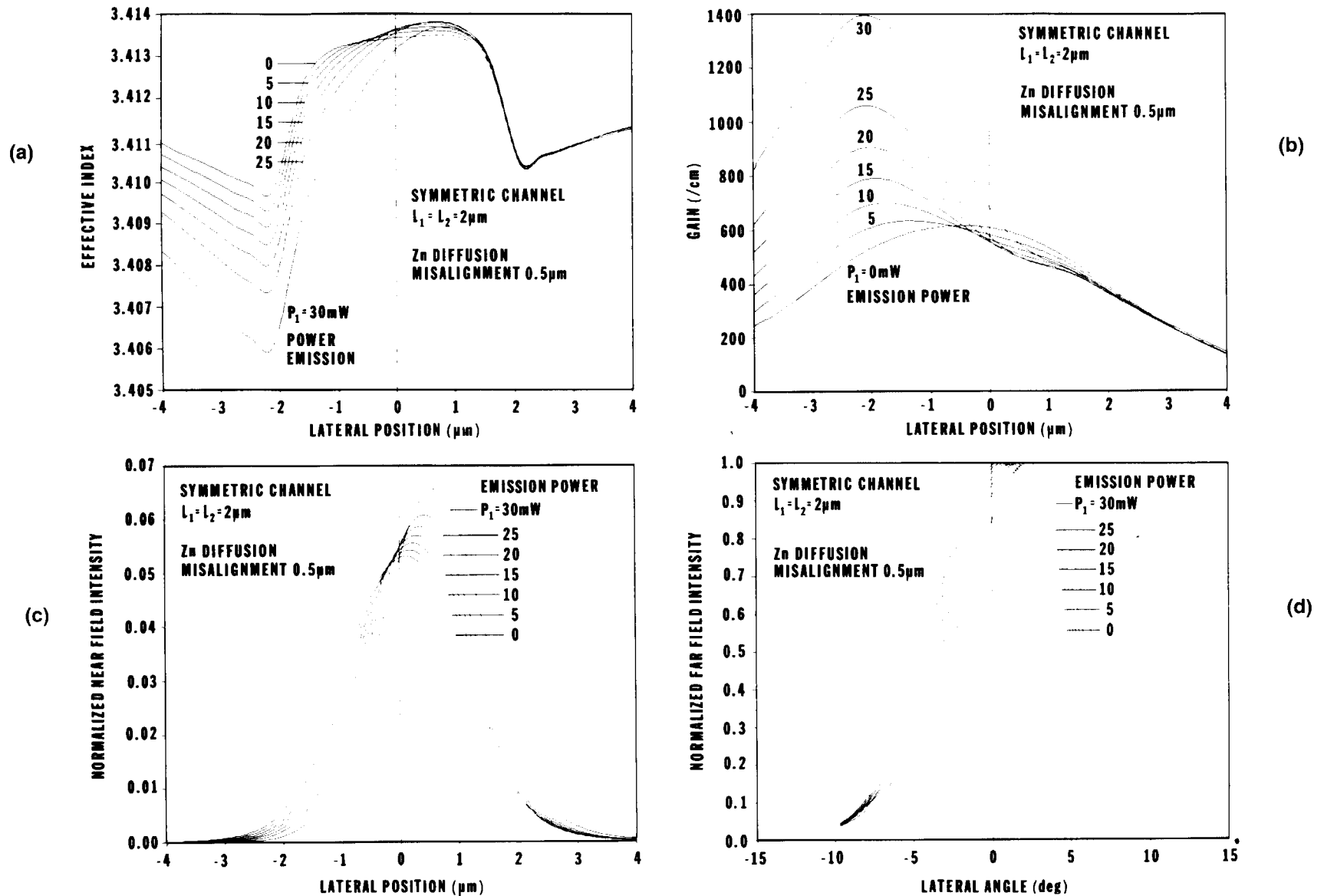


Figure II-17. Calculated (a) lateral effective index profiles, (b) lateral gain profiles in the active layer, (c) near-field intensity distributions, and (d) far-field intensity patterns for a symmetric CSP-DH structure ($l_1 = l_2 = 2.0 \mu\text{m}$), with a misaligned $4\text{-}\mu\text{m}$ -wide Zn diffusion front for output powers of 0, 5, 10, 15, 20, 25, and 30 mW. The Zn diffusion is misaligned by $0.5 \mu\text{m}$.

Section III

CSP ARRAY FABRICATION AND MOUNTING

GROWTH

CSP

An automated LPE growth system used for the fabrication of the CSP lasers. A photograph of this system is shown in Fig. III-1. In addition, we reported on a new boat design and discussed growth techniques that provided layers with more uniform thickness and with greater reproducibility. The CSP structure is fabricated in a single-growth-step using LPE. V-shaped channels are chemically etched in the (100) oriented GaAs substrate along the [011] direction using an oxide-defined contact mask before LPE growth. Prior to placement of the substrate in the horizontal sliding graphite growth boat, the entire surface of the wafer is subject to a light chemical etch. This procedure ensures that both the surfaces in the channel region and on the substrate are chemically prepared in the same manner for LPE growth.

ORIGINAL PAGE
BLACK AND WHITE PHOTOGRAPH

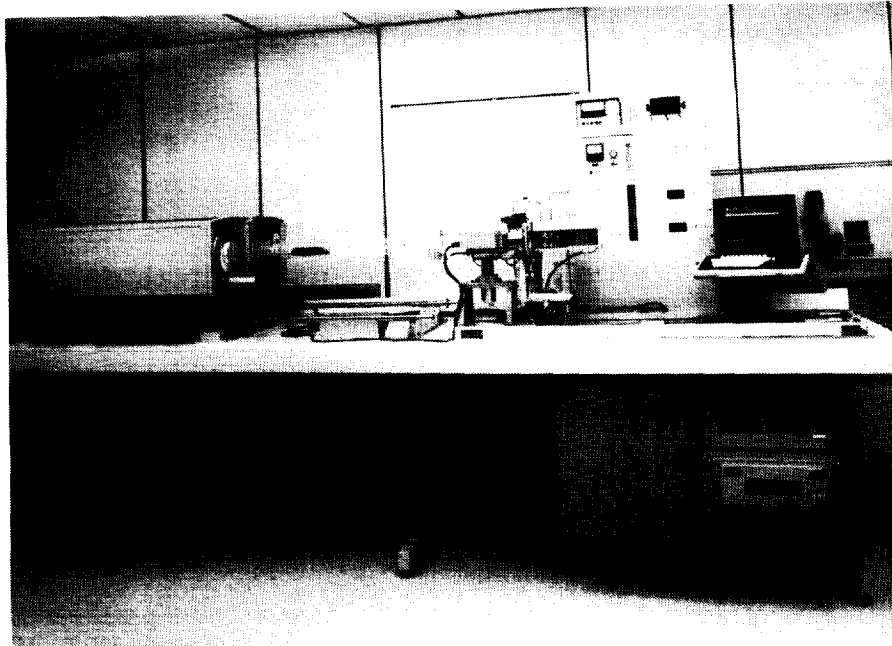


Figure III-1. LPE reactor used for growth of CSP lasers.

LPE growth is performed over the V-channeled substrate and four layers are grown: (1) $\text{Al}_x\text{Ga}_{1-x}\text{As}$ cladding layer ($x = 0.27$, $0.3 \mu\text{m}$, $N_d = 1 \times 10^{18} \text{cm}^{-3}$); (2) GaAs active layer ($0.07 \mu\text{m}$, $N_d = 1 \times 10^{17} \text{cm}^{-3}$); (3) $\text{Al}_x\text{Ga}_{1-x}\text{As}$ cladding layer ($x = 0.27$, $1.5 \mu\text{m}$, $N_a = 5 \times 10^{17} \text{cm}^{-3}$); (4) GaAs capping layer ($0.7 \mu\text{m}$, $N_d = 5 \times 10^{17} \text{cm}^{-3}$). The growth is performed at 800°C using a cooling rate of $1^\circ\text{C}/\text{min}$. The fabrication of high-power CSP lasers having the proper lateral index profile for fundamental mode operation requires the active layer to be planar over the V-channel while the thickness of the n-cladding layer outside the channel region is maintained between 0.2 and $0.5 \mu\text{m}$. A non-planar active layer alters the lateral index profile of the CSP structure, which degrades. To ensure planar active-layer growth over the channel region, it is necessary to maximize the total amount of supercooling associated with the gallium melt used for the growth of the n-cladding layer. This is accomplished in our automated growth system by using the single-phase growth method [18] for the n-cladding layer and the two-phase method [18] for the growth of the other layers in the CSP structure. The single-phase growth method permits us to accurately control the degree of supercooling present in the gallium melt prior to the introduction of the growth wafer. In addition to the quick filling of the V-channel to planarize the layer, careful control of the amount of supercooling also permits a high degree of control on layer thickness not only across the wafer but from one LPE growth run to another. The single-phase growth technique may also be used for the growth of the other layers in the structure, but is not necessary since the n-cladding layer grown directly on the non-planar substrate planarizes the surface for the subsequent layers. The use of the single-phase growth technique for all the layers in the structure would unnecessarily complicate the growth process.

Another factor affecting the planarity of the active layer in the CSP structure is the crystal orientation of the growth substrate. The effects of surface morphology due to substrate misorientation with respect to the (100) surface have been discussed. We have reported that substrate misorientations may result in terracing of the n-cladding and active layers in the CSP structure during LPE growth. Thus, the shape or planarity of the epitaxial layers are extremely sensitive to such factors as the non-planar growth surface, substrate orientation, and growth conditions. Independent of the growth conditions and/or the geometric channel shape, the terrace or perturbation in the layer would eventually be eliminated as the (100) surface, which possesses the lowest interfacial energy density, is reconstructed. However, in the CSP structure the

terrace must be eliminated before the growth of the active layer, otherwise the change in the active layer thickness due to the terrace alters the lateral index profile of CSP structure. By optimizing the LPE growth conditions and minimizing the misorientation of the growth substrate with respect to the (100) plane, planar active layer growth can be obtained on a routine basis.

A terrace formed in the active layer of the CSP structure cannot be observed in standard, high-magnification cross-sectional micrographs. A more effective examination technique is angle lapping of the growth surface. A 1° angle lap polished perpendicular to the active layer can reveal terracing as small as 10.0 nm. Figures III-2a and III-2b are 1° angle lap micrographs of two CSP growth runs displaying a terraced and a non-terraced active layer, respectively. The height of the terrace or step in Fig. III-2a is approximately 60.0 nm, which yields a 20% change in the active layer thickness. Thus, this terrace represents a significant change in the properties of the CSP structure. A CSP laser with a planar active layer is depicted in Fig. III-2b. Laser devices fabricated from this wafer displayed low threshold operation, kink-free P-I curves to high output powers, fundamental mode operation, and stable far-field radiation patterns, while devices fabricated with the terraced active layers displayed kinks in the P-I curve and far-field radiation patterns that move with changing drive current. Thus, careful control of the V-channel etching, substrate orientation, and LPE growth can lead to the fabrication of CSP lasers having desirable performance properties. The flow of current in the CSP structure is confined to the channel region via a deep zinc diffusion. Zinc is diffused through the n-type cap layer into the p-type cladding layer using an oxide-defined contact mask, thereby forming a reverse bias p-n junction to confine the current flow. The leading edge of the zinc front is positioned approximately $0.5 \mu\text{m}$ above the active layer.

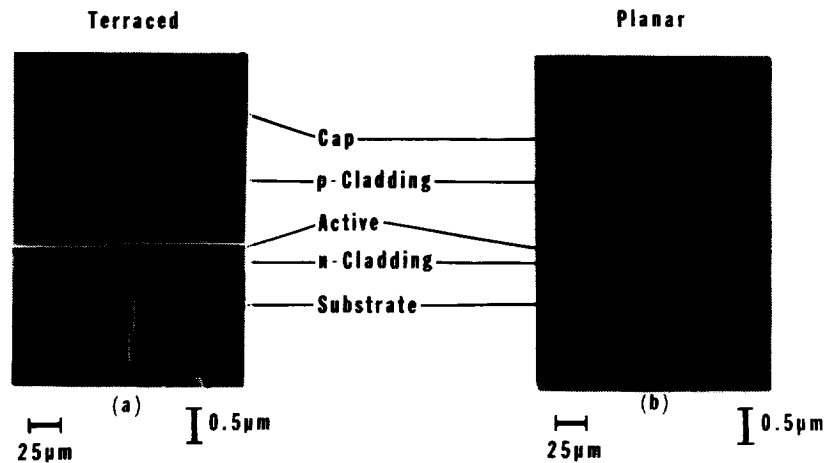


Figure III-2. Micrograph of CSP growth angle lapped at 1° angle showing (a) terraced active layer and (b) non-terraced active layer.

2. DCC-CSP

Although significant improvements have been made to the CSP structure that have resulted in devices exhibiting lower threshold currents and record efficiencies, further refinements are possible to reduce the drive level during operation. Our modeling studies indicated that the incorporation of one or more buffer/current blocking layers to effectively focus the current to the lasing area should provide devices with improved differential quantum efficiencies. The incorporation of the buffer/current blocking layers into the CSP structure would require that a second-growth step be added to the fabrication procedure. In addition, a photolithographic process must be performed on top of this layer(s) to facilitate etching of the V-channels. Past experience in other programs in which high-resolution photolithography was required has demonstrated that surface morphology was extremely important in terms of contacting the mask used in the photolithographic process. Although the surface morphology obtained in the LPE growth process can be quite good, the edge effects around the perimeter of the wafer due to the growth can result in large hillock formation. In order to facilitate good contacting during the photolithographic process it is necessary to remove the edges from the grown substrate and only use the central portion for the growth of the CSP structure. This additional LPE process will double the amount of growth time necessary for fabricating the CSP structure and will reduce the throughput from our reactor.

Recently, we have developed a metalorganic chemical vapor deposition (MOCVD) process for the growth of AlGaAs and GaAs films. MOCVD is an open tube vapor-phase epitaxial growth process. This means that the flowing reactant gas stream only contacts the growing surface once. After the stream passes the crystal, the reactants do not participate in the growth process. Efficient deposition of material, thus, requires that a high degree of supersaturation exist over the growing crystal surface. This condition can be established by ensuring that the reactants have high partial pressures in the gas stream. The supersaturation condition is relieved upon contact with the substrate, where the reactants are deposited on the growing crystal and the gas stream leaving the substrate is in equilibrium with the deposited film at the substrate temperature. The partial pressures of the reactants in the gas stream leaving the reactor are reduced by the amount of the reactants deposited on the crystal surface. Since the reactants remaining in the gas stream are now discarded, most efficient deposition occurs when the highest degree of supersaturation is present. A photograph of our MOCVD reactor manufactured by EMCORE Corporation is shown in Fig. III-3.

ORIGINAL PAGE
BLACK AND WHITE PHOTOGRAPH

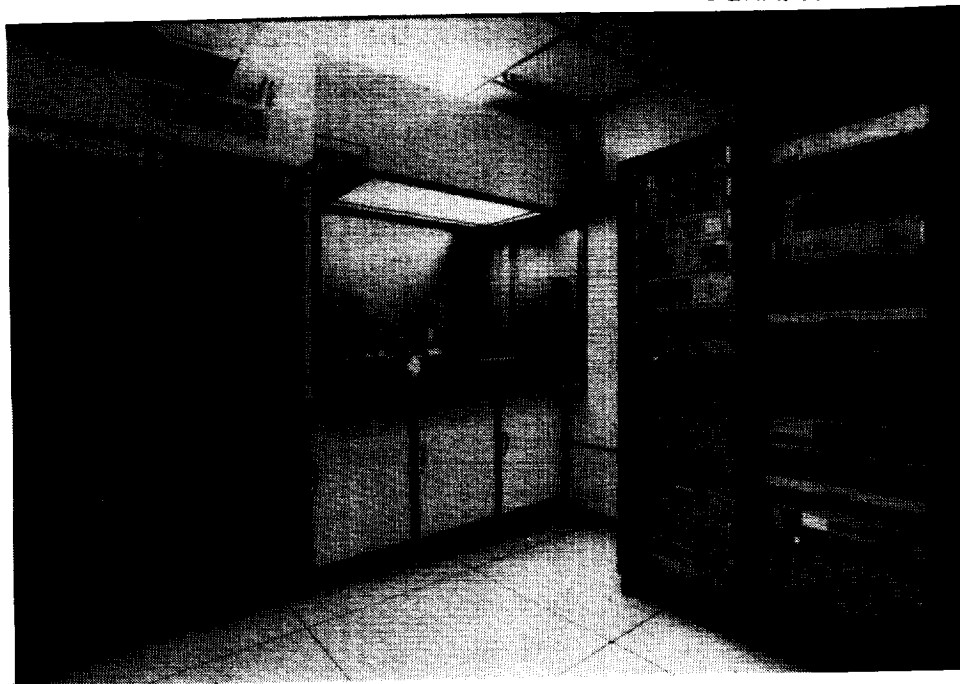


Figure III-3. MOCVD reactor.

B. PROCESSING

The processing steps involved in CSP and other laser diode fabrication is straight forward. However, much care and effort must be spent to ensure adequate yield. In view of the low yield we have experienced recently, we have reviewed our processing techniques, bearing in mind the areas that need improvement. We distinguish two processing clusters following growth. The front-end processing, which includes the steps prior to zinc diffusion, and the back-end processing, which starts with zinc diffusion. The front-end steps are outlined in the flow chart of Fig. III-4 and are illustrated step-by-step in Fig. III-5. The back-end steps are described below. Although the back-end processing steps are well established, we will follow the description of the process with a discussion of those parts of the process where modifications may have a significant impact on the yield and reliability of the final product.

The general process flow is shown in Fig. III-6. The first processing step is the deposition of a thin layer (120 nm of silicon dioxide, which will serve as a zinc diffusion masking layer). Prior to oxide deposition the wafer is cleaned in an etch composed of NaOH and hydrogen peroxide in DI water. The silicon dioxide is deposited at 350°C by chemical vapor deposition. To enhance the adhesion of this oxide so that it will be effective in limiting the lateral zinc diffusion, the oxide is densified by a two hour bake at 800°C in a hydrogen ambient.

Standard photolithographic techniques are then used to define the oxide stripes or cuts in the oxide, using positive photoresist (AZ 1375). After exposure and development of the pattern using a nominal 5 μm stripe width mask, the oxide is etched in a CF_4 plasma etcher. The photoresist is then removed by plasma stripping in oxygen.

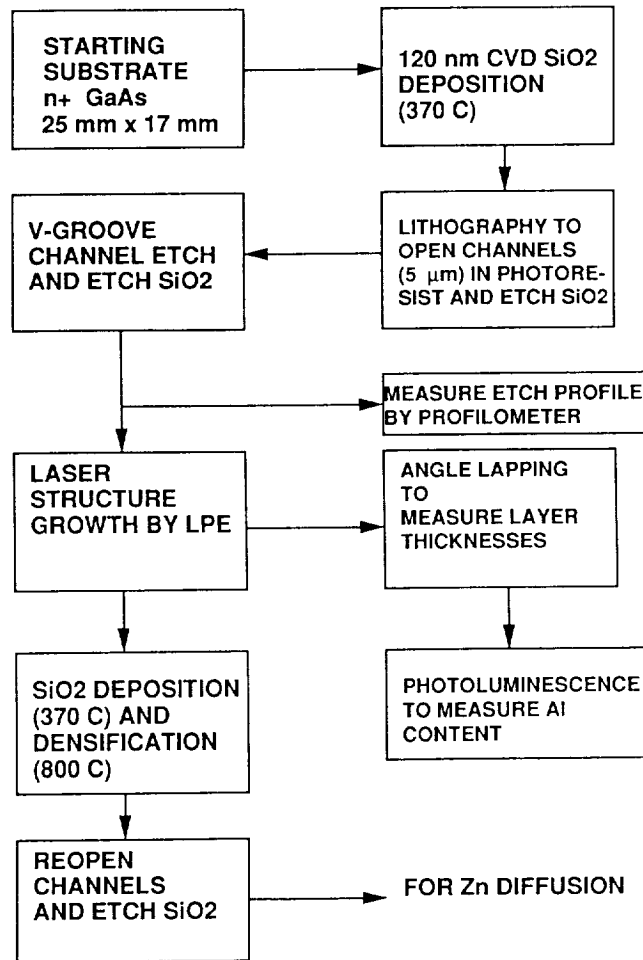


Figure III-4. Front-end CSP processing flow chart.

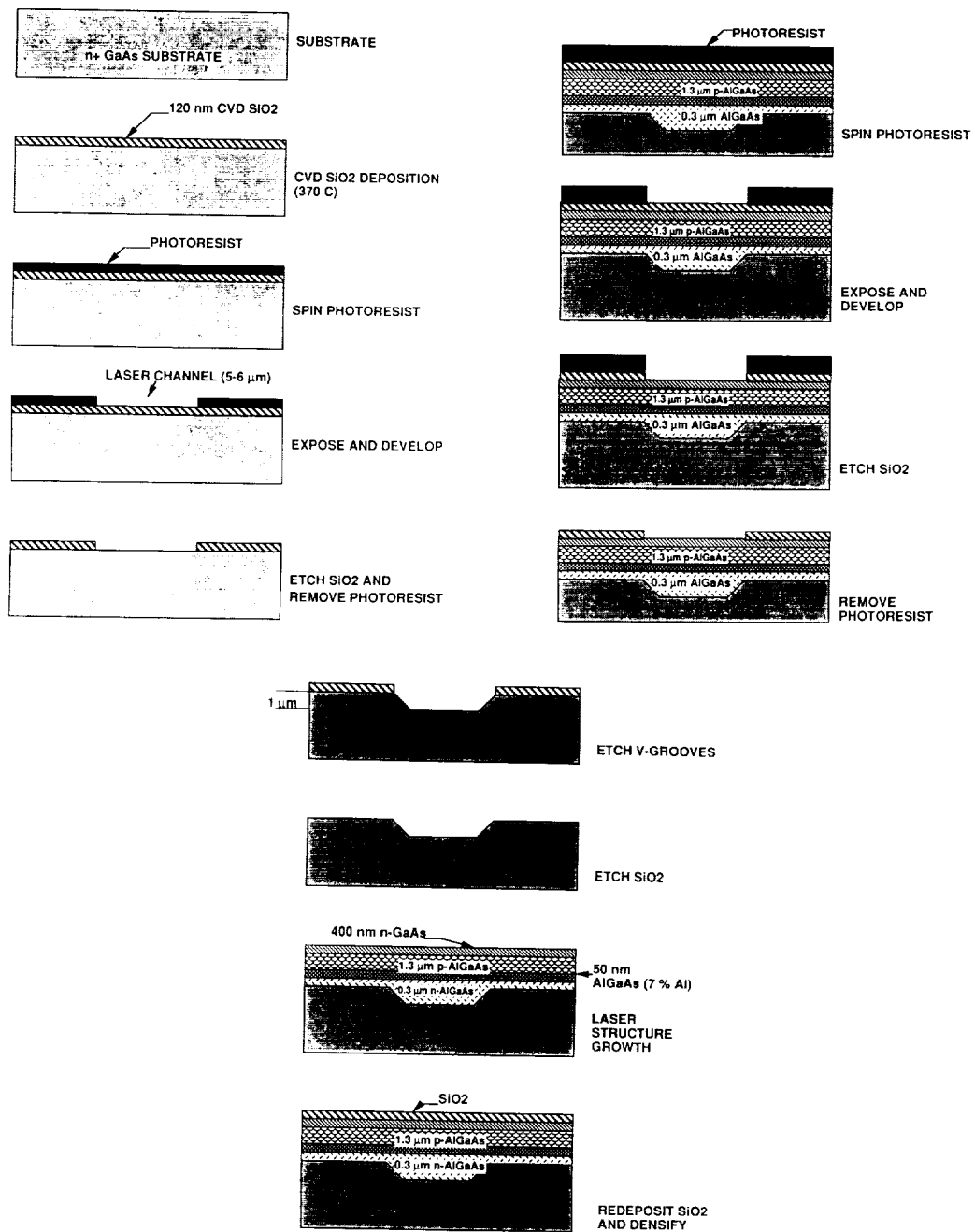


Figure III-5. Front-end CSP fabrication step.

ORIGINAL PAGE IS
OF POOR QUALITY

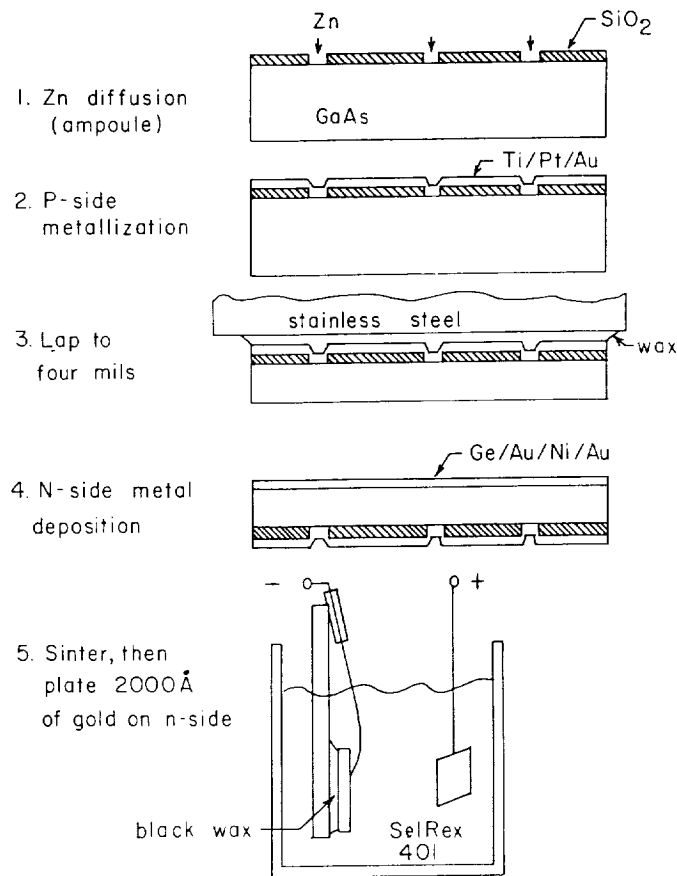


Figure III-6. Back-end processing steps for CSP fabrication.

Zinc diffusion is used to convert the conductivity type to p-type within the oxide opening to establish the conductive path to the active layer of the laser. The zinc diffusion creates a highly doped p-type surface layer that allows a low resistance ohmic contact to be formed by depositing a Ti/Pt/Au metal layer. The diffusion takes place in a sealed quartz ampoule containing a mixture of ZnAs₂ and powdered GaAs, which establishes an arsenic overpressure to prevent dissociation of the exposed wafer surface at the furnace's temperature. Native oxides on the wafers are removed before the zinc diffusion by cleaning in a solution of HCl and DI water. The depth of the zinc penetration is controlled by the diffusion time. This is a critical parameter because the zinc must penetrate the n-type capping layer but not reach the active channel of the laser.

After removal from the ampoule, a small section of the wafer is cleaved off and stained to verify the position of the zinc front and to measure its lateral spread. Prior to the p-metal deposition, the wafers are cleaned by etching in a dilute solution of ammonium hydroxide, H₂O₂, and DI water. Our standard

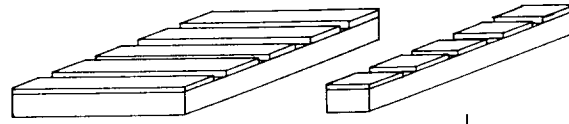
p-contact ohmic metallization consists of platinum, titanium, and gold layers that are E-gun evaporated onto the wafers.

Individual lasers are now electrically isolated by ion beam milling to a depth of about 2- μm a 50- μm wide channel through the p- contact metallization and all the active device layers, using a photoresist mask pattern.

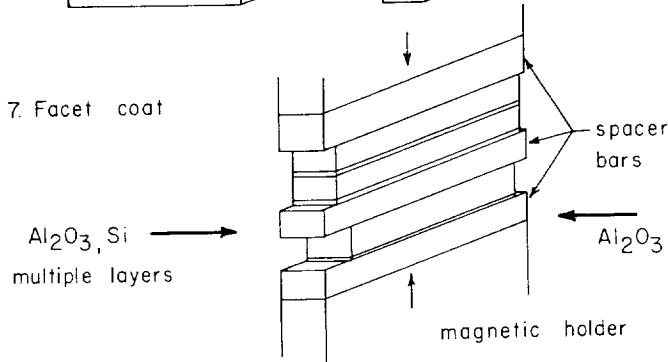
The wafers are thinned down by mechanical lapping, and electrical contact to the n-type layers is made by depositing a gold germanium-based metal system and sintering at 450°C. To decrease the spreading resistance of the n-contact and provide a fresh layer of gold for good bonding, a 100 nm additional layer of gold is electroplated on top of the sintered metal.

This completes the basic process to fabricate the laser structure. The remaining steps involve cleaving the wafer into bars, thereby defining the cavity length, and producing the end facets. These steps are outlined in Fig. III-7 to produce bars, the wafers are scribed for a short distance at one edge with a diamond tipped scribbing machine that automatically repeats the scribe marks at the distance set for the cavity length. The actual cleaving operation is done in a "cracker", which has a flexible wafer support stage and a metal roller that propagates the cleave along the full length of the wafer. The facet coatings consist of an anti-reflection coating on one facet (output facet) and a highly reflective coating on the opposite facet. The anti-reflection coating consists of a quarter wavelength thickness of Al_2O_3 . The reflective coating is comprised of a six-layer stack of alternating layers of Al_2O_3 and silicon. Each of these layers is also a thickness representing a quarter wavelength considering the refractive index of the respective materials. The final process step is to cleave the bars at right angles to the facets to produce individual ten-element arrays. This is performed in a machine called a chipping scriber. This type of scriber is similar to dicing machines except that the diamond tool makes a short pivoting motion to scratch the surface of the bar only along a short span between the facet faces. This prevents damage to the coatings. After the scribe marks are made the arrays are carefully separated by cleaving the bars with a manual cleaving tool.

6. Cleave into bars



7. Facet coat



8. Chip bars into lasers

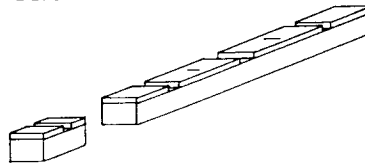


Figure III-7. Cleaving, facet coating, and chipping.

C. PROCESS MODIFICATION FOR IMPROVED RELIABILITY

The previous section described in some detail the present fabrication process. There are several areas in which changes in the process may make a contribution to improved fabrication yield laser lifetimes. The first modification would be to replace the silicon dioxide layer with a dielectric, such as silicon nitride, which has a 16 times greater thermal conductivity. Table III-1 contains a list of the thermal conductivities of the materials used to construct the laser. The thermal conductivity of silicon dioxide is by far the lowest of all the materials employed.

Although it is only 120 nm thick, an analysis of a similar structure by Nakwaski [19] showed that the oxide layer effectively confines the thermal path to that of the opening in the oxide. The result of Nakwaski's analysis are illustrated in Fig. III-8 in which heat flux from the active laser area can reach the heatsink either through the oxide opening (1) or through the oxide (2) or spread out laterally then return and exit through the oxide opening. With silicon dioxide

layers, heat paths 1 and 3 dominate, significantly increasing the thermal impedance.

Table III-1
Thermal Conductivities Of Materials In AlGaAs Diodes

<u>Material</u>	<u>Conductivity (W m⁻¹ k⁻¹)</u>
GaAs	47
Al _x Ga _{1-x} As (x= 0.3)	12.8
Ti	22
Pt	73
Au	318
In	87
Cu	400
SiO ₂	1 to 1.4
Si ₃ N ₄	16 to 32

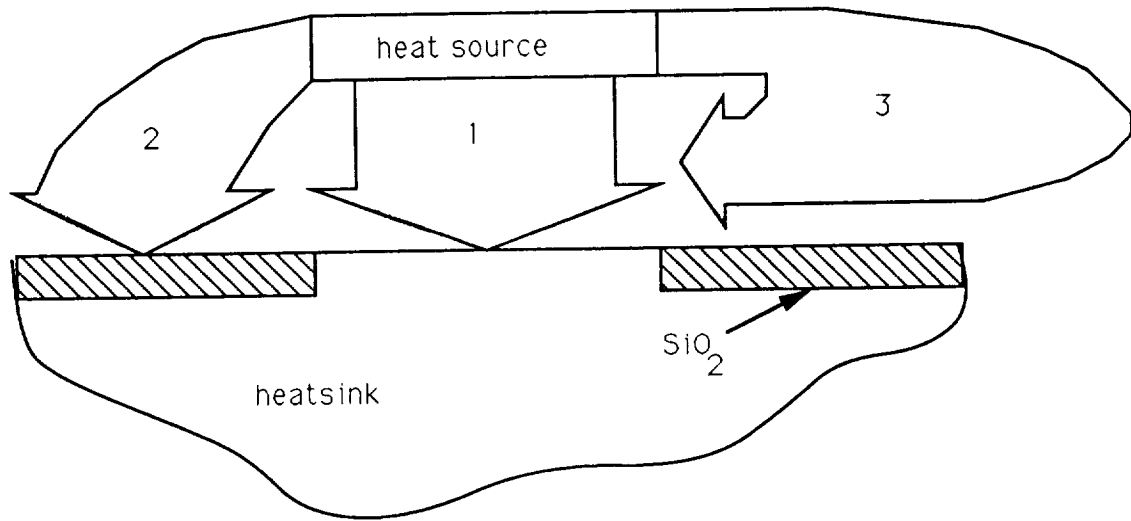


Figure III-8. Heat flow model of Nakwaski. (1) Directly through stripe contact. (2) Flowing far from source to reach heat silk through oxide layer. (3) Flowing through regions far from heatsink, but reaching heatsink through stripe. "The oxide layer, ... effectively confines heat spreading in the lateral direction."

One can think of a great number of process modifications that may affect the device reliability. The Ishikawa (cause and effect) diagram in Fig. III-9 lists several types of defects that can occur in the process. We have plans to investigate several process variations. We have discussed the replacement of silicon dioxide for thermal reasons, but another benefit would be the removal of the 800°C densification bake. This is likely to introduce gallium vacancies by out-diffusion of gallium into the oxide. Another source of damage may be the lapping step in which subsequent stresses may cause dislocations to migrate into the active layer. Therefore, it may be of benefit to follow the lapping with a chemical etch or polishing step to remove the lapping damage. These variations and others will be investigated in the near future to improve the yield and longevity of these edge emitting laser structures.

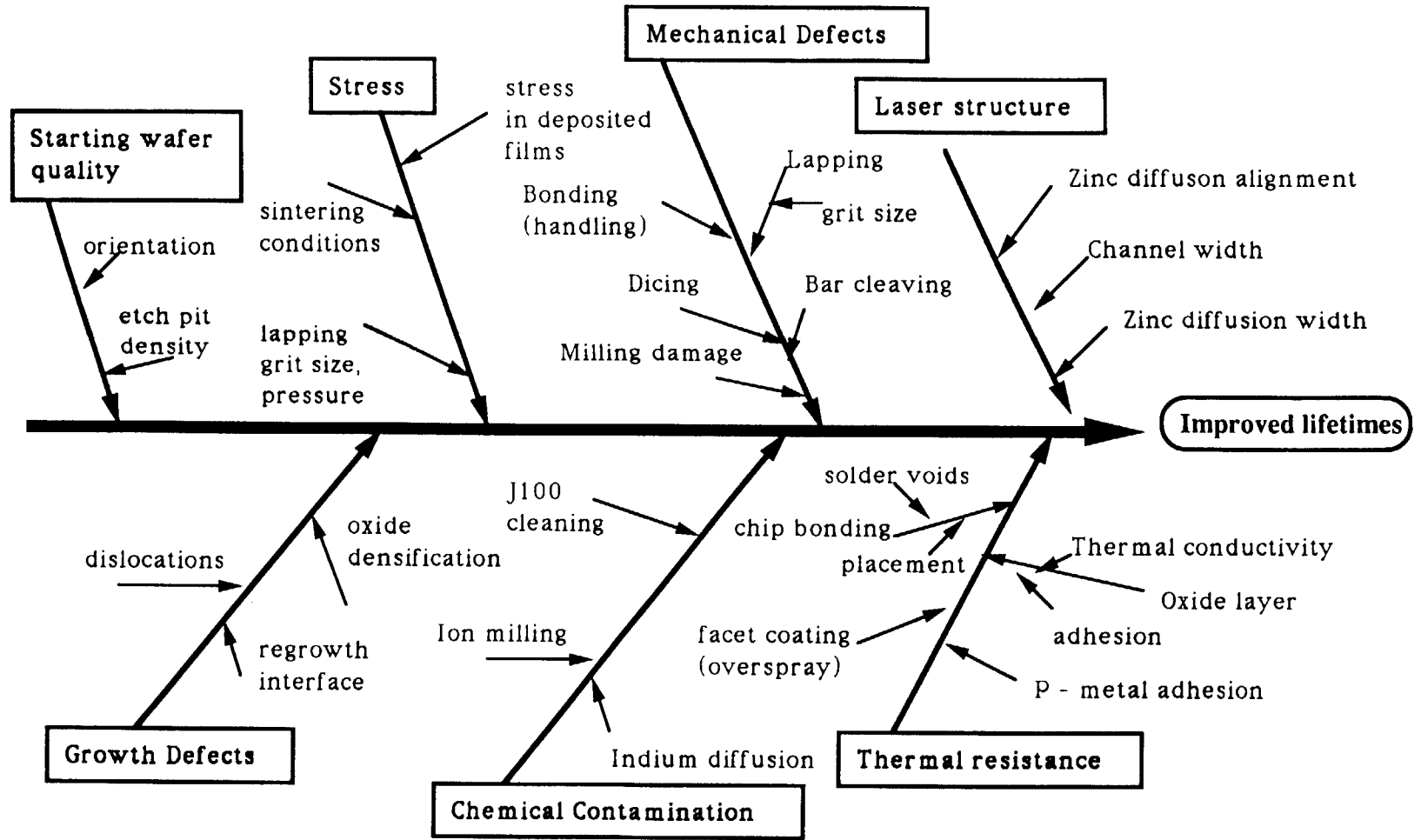


Figure III-9. Ishikawa's cause and effect diagram for diode reliability.

D. MACHINE-ASSISTED MOUNTING OF LASER ARRAYS

To date, most of our high-power AlGaAs diode lasers have been bonded to submounts by hand using indium solder. While this has sufficed for developmental purposes, manual mounting of diode lasers and arrays of diode lasers is not desired for mass production of devices, where repetitive, accurate chip placement is required. In addition, indium has a low softening temperature and has shown a tendency to creep and migrate. These effects can cause electrical shorting (and failure) of the laser. The use of indium also requires the application of flux and cleaning solvents. These are potential contaminants that can degrade laser performance after a period of time. These considerations strongly suggest the use of machine-assisted mounting of high-power devices using fluxless, higher temperature bonding materials. Such techniques have been under investigation at the David Sarnoff Research Center since 1983. The problem is a difficult one, especially when applied to long arrays. Arrays are more susceptible to differential stresses developing across the length of the chip. These stresses can induce curvature in the long devices, making the attainment of a good, uniform bond more difficult than in the case of short individual diode lasers, and certainly making the chip more fragile. With these considerations in mind, we have continued our explorations of machine bonding techniques and metallurgies using the single lasers with the objective of applying these techniques to individually addressed arrays.

Our baseline approach was to develop a machine-assisted, fluxless die mounting process using electroplatings of tin, 2 to 8 μm thick, on the metallized electrodes of the array submount. The wetting of the tin was enhanced by the use of an additional thin layer of nickel on the metallized electrodes. Furthermore, a layer of gold, 1000 \AA thick, was added on top of the tin to prevent the formation of tin oxide. Precise control of electroplated layers of tin and gold result in the desired proportions of gold and tin in the final solder layer alloy, which is a combination of the electroplated tin and gold and the gold on the laser chip. Excellent wetting characteristics of the tin and gold has helped achieve high quality fluxless bonds.

The laser-array chip is bonded to the BeO submount by using a "rack-and-stack" assembly approach. According to this method, the BeO submount is securely held in a specially designed fixture, as shown in Fig. III-10

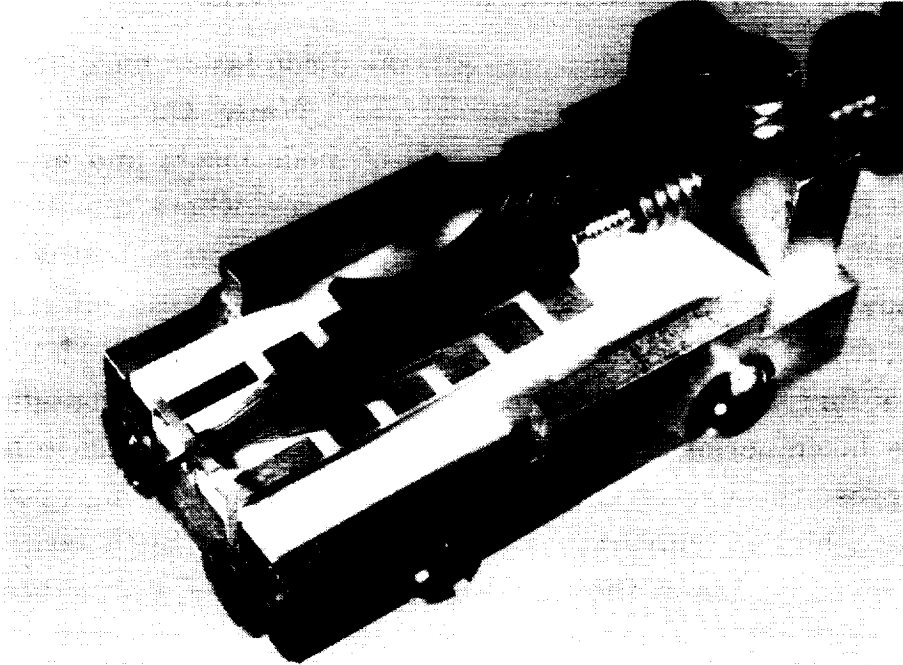


Figure III-10. Fixture for machine-assisted bonding of diode arrays.

Both the laser chip and the BeO submount are butted up against a slotted quartz plate attached to the front end of the fixture (left side in Fig. III-10). A spring applying pressure on the n-side of the chip keeps it in intimate contact with the solder metallized copper fingers on the BeO. Alignment is done under a microscope looking through the slot in the quartz plate. The alignment fixture is placed on a heating plate inside a chamber filled with a nonoxidizing gas mixture of 80% nitrogen and 20% hydrogen. The solder temperature is raised above melting point and then the assembly is cooled to finish the bonding. The bonded device is then removed from the fixture and, since there is no flux used, it does not require any cleaning or rinsing in solvents. A thin gold wire is ultrasonic-wedge bonded to the n-side of the laser chip for electrical connection.

Figure III-11a shows an array containing seven good diodes bonded using the fluxless gold-tin mounting technique. This device, as can be seen, has three gold wires bonded to the n-side for extra reliability. Figure III-11b) is the front view of the same device showing the front facet. Excellent alignment is evident from the nine bright spots between the ten solder bonds, which are the ion-milled isolation channels in the array.

ORIGINAL PAGE
BLACK AND WHITE PHOTOGRAPH

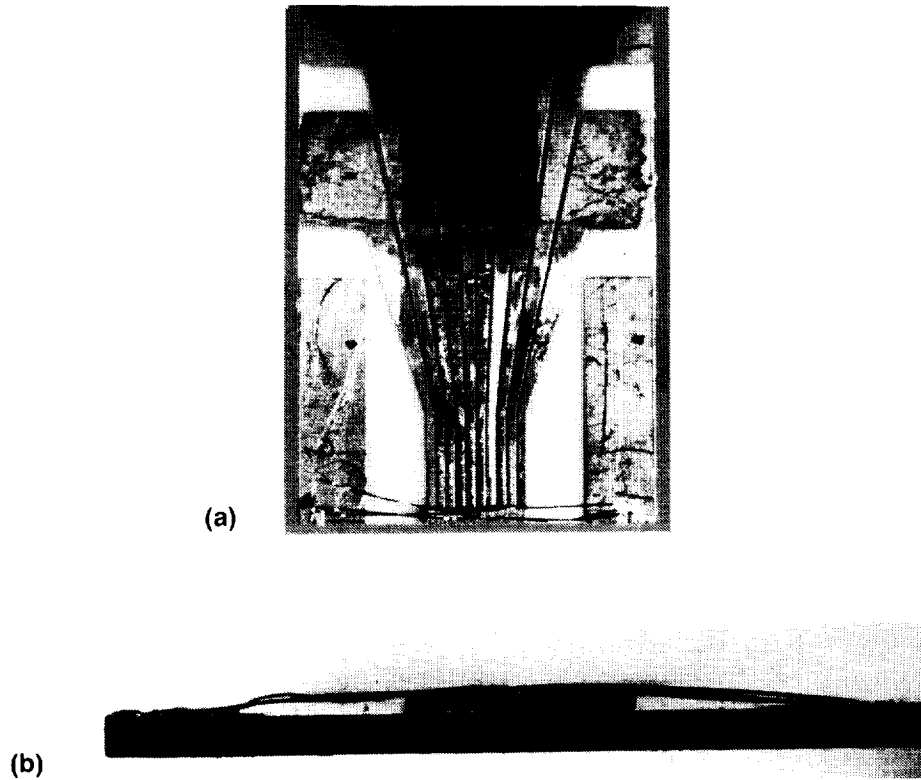


Figure III-11. (a) Array containing seven lasers bonded by fluxless machine-assisted method using gold-tin bond. (b) Front facet of array containing seven lasers bonded by fluxless machine-assisted method using gold-tin bond.

The P-I characteristics of the bonded array is shown in Fig. III-12. All the diode elements showed characteristics to 30 mW cw in a manner that was consistent with probe testing data. Their performance was also similar to diodes hand-mounted with indium solder and flux.

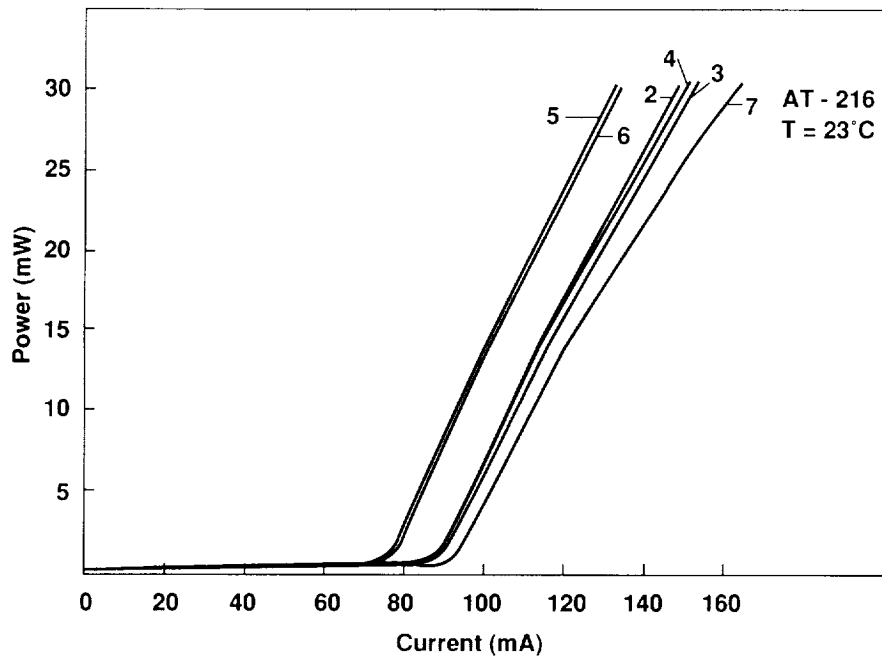


Figure III-12. P-I characteristics of seven-laser array bonded by fluxless machine-assisted methods.

More work is needed on this approach before we start using it routinely in place of the hand mounting approach, and there are several issues to be understood. For example, we have found that bonding can cause stresses that affect the threshold current density. Stress is induced by the type of solder used to bond the array. We have investigated this issue as part of the development of our machine-assisted bonding process. Soft solder, such as indium, can creep and allow for the relief of stress. Harder solders, such as gold-tin, do not allow such relief without annealing. In general, the threshold current decreases for compressive stress and increases for tensile stress.

Section IV

I-CSP ARRAYS

In Section II, we described certain tolerance problems associated with CSP. That structure also suffers from the fact that it can only be grown by LPE, the only growth technique that can be used for uniform planar layers over non-planar substrates. However, LPE-grown layers are not uniform in thickness, and composition and repeatability is poor. On the other hand, MOCVD does not cover steps very well. The growth process is more complex, the equipment is more expensive, and it uses toxic products. However, the growth is uniform and reproducibility is excellent. Both DH and quantum well (QW) structures can be grown by this technique, and QWs offer the distinct advantage of higher efficiency, hence, reduced heating. Furthermore, it can be used to make 780 nm lasers, should such devices prove to be desirable for increased recording packaging density.

The I-CSP structure lends itself well to MOCVD growth, and it is shown in Fig. IV-1 for a DH laser array. The QW structure is obtained by substituting the QW and confining layers for the active layer.

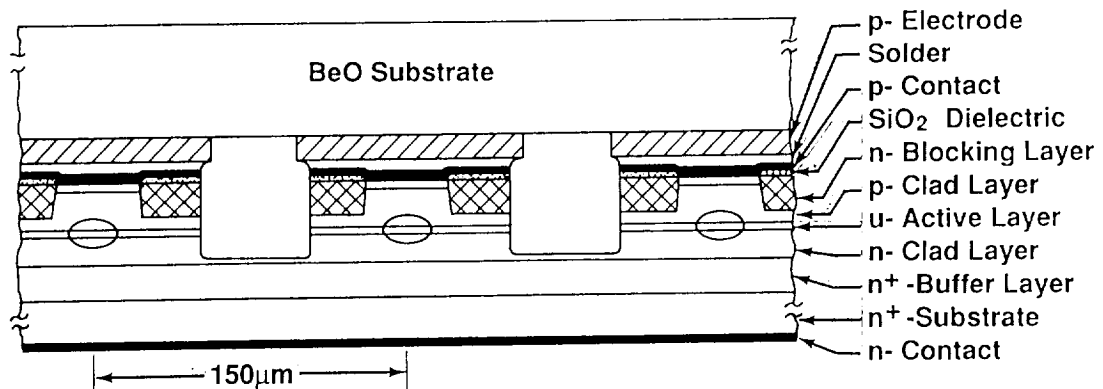


Figure IV-1. Monolithic double heterojunction I-CSP array. The QW structure is obtained by substituting the QW and confining layers for the active layer.

In this structure, all the layers are grown as for any simple planar double heterostructure laser. A ridge is then created by photolithography, then by etching the p-cap and part of the p-confinement layer. This ridge is functionally the inverse of the CSP V-groove. At this point, the structure is that of an ordinary index-guided ridge laser, and samples can be tested to evaluate threshold current and efficiency. It is recalled that stable guiding in the CSP is obtained by means of loss in the wing of the optical field does to absorption in the GaAs substrate. The same principle is obtained in the I-CSP but with regrown GaAs layer (the crossed region in Fig. IV-1). This layer is also n-doped so that it provides both the loss mechanism characteristic of CSP and current blocking for lateral current confinement. The cap on top of the ridge can be a heavily doped p-GaAs material, thus eliminating the need for zinc diffusion. The structure is also self-aligned, i.e., the gain profile is automatically centered over the ridge by virtue of the design configuration.

The steps required to fabricate I-CSP arrays are outlined in Fig. IV-2. We have made ridge SCH-SQW laser arrays, i.e., I-CSP arrays without the regrown blocking layer, and found them to have the lowest threshold current we have ever observed for arrays, as can be seen from the P-I characteristics in Fig. IV-3.

The far-field pattern of the ridge QW diode is shown in Fig. IV-4. The perpendicular full width half maximum (FWHM) is about 42° for the structure tested. This is larger than the required 30° FWHM for optical recording. The broader perpendicular pattern is due to the SCH layers thicknesses, which in this case caused the vertical mode size to be too small. The spot size must be made larger in order to reduce the far-field divergence. We are now growing material to investigate the trade-offs involved in increasing spot size. However, it is expected that the required modifications in the SCH and QW layer thicknesses will increase threshold current density and reduce efficiency.

The trade-offs will also require investigation of DH structures. DH MOCVD grown structures, with relative thin active layer (400\AA to 600\AA), are attractive for high power laser applications. The threshold is higher than for QW, but lower than LPE-grown structures. More importantly, the perpendicular far-field divergence is within the 30° range required for the spaceflight optical disk recorder (SODR) being supported by NASA.

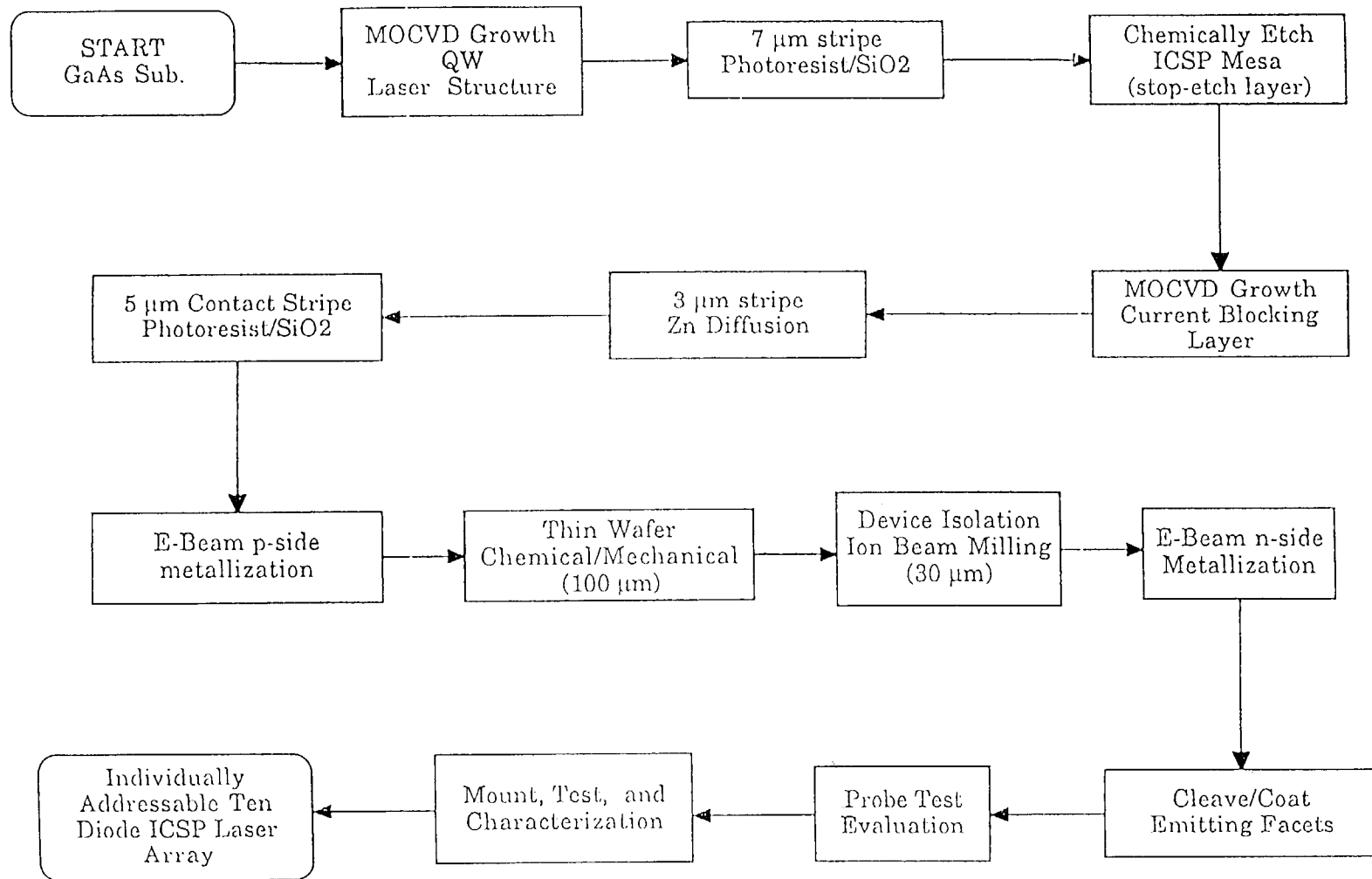


Figure IV-2. Process steps for I-CSP arrays.

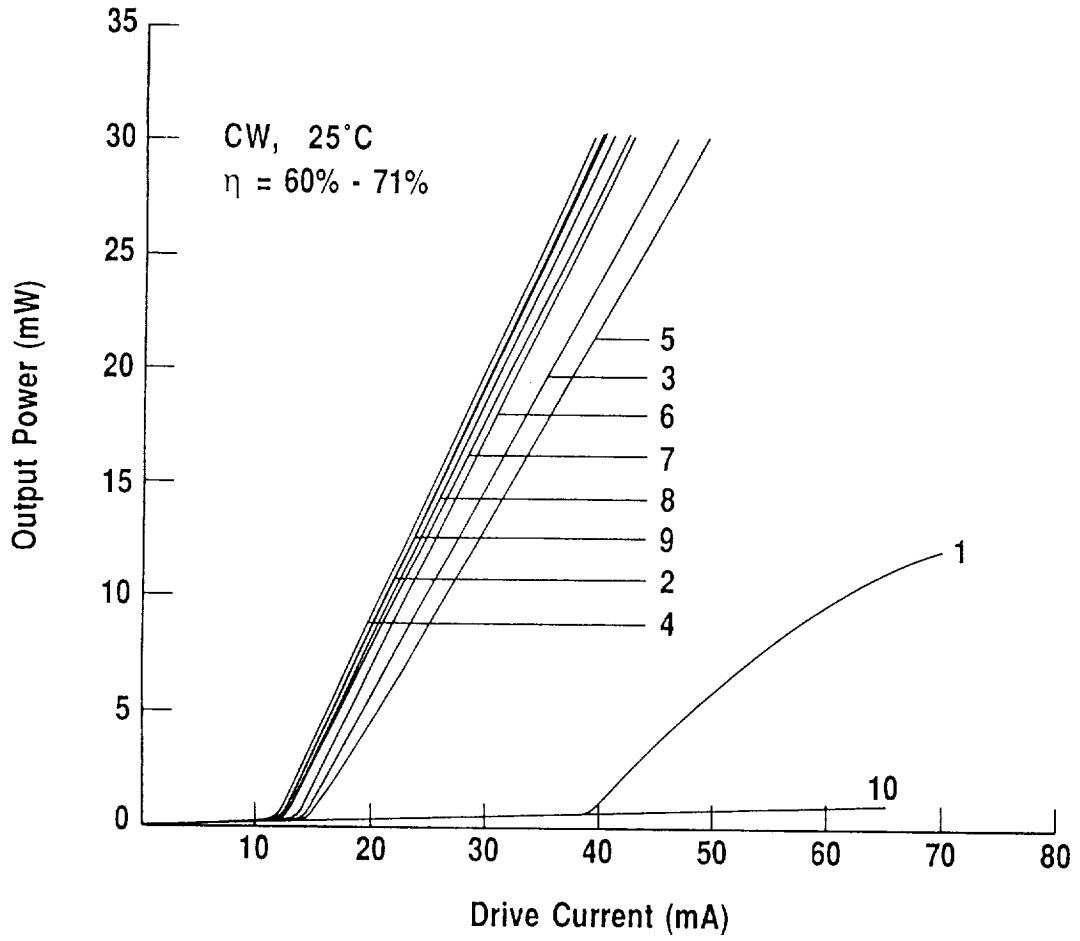


Figure IV-3. A ridge QW laser diode array.

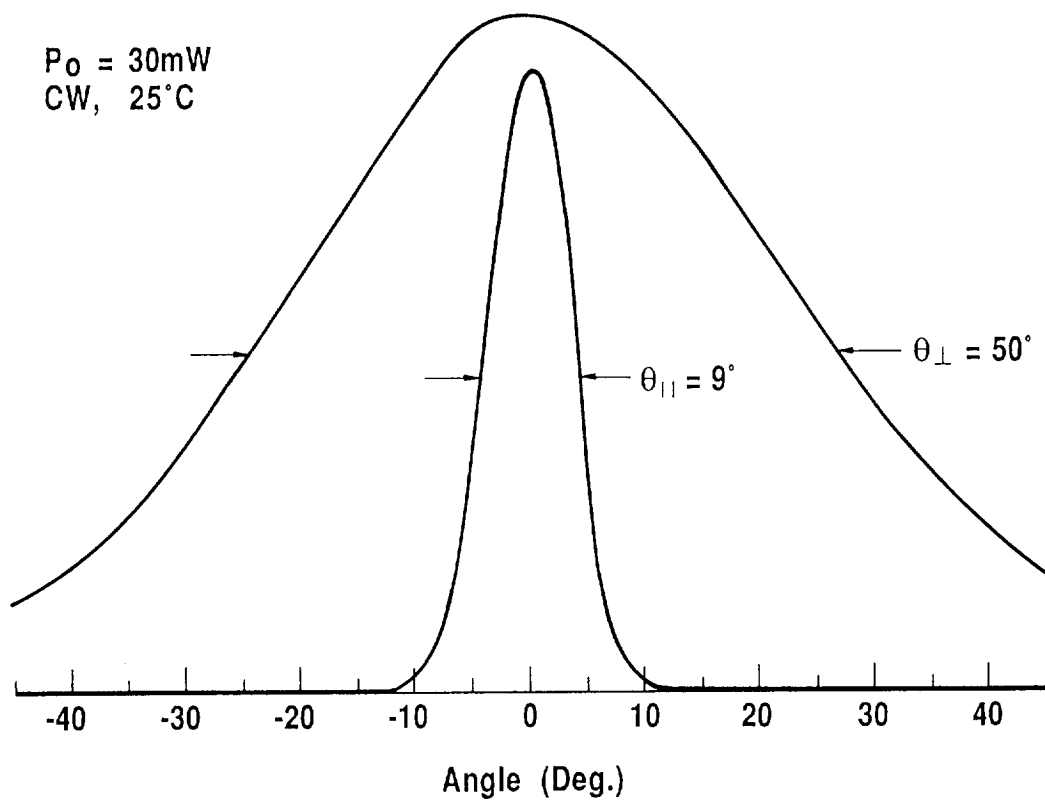


Figure IV-4. Far-field pattern of ridge QW laser array.

Section V

TECHNIQUES FOR ENHANCED OPERATION OF MAGNETO-OPTIC SYSTEMS

A. FEEDBACK ANALYSIS

The laser diode parameters are of considerable importance in establishing the performance of MO systems. In addition to the requirements of high power, narrow spectral spread, and low astigmatism, the noise characteristics of the lasers have emerged as critical with respect to the system's ability to readout data while maintaining a prescribed error rate (typically 10^{-9} to 10^{-12}). The bit error rate (BER) is determined by the signal-to-noise (SNR). There are several noise components in a MO storage system, many of which are common to all optical data storage systems. They include the amplifier noise, shot noise, disk noise, and laser noise. Disk and laser noises are the largest components and affect the MO readout more strongly than any other system. Typically, the readout light incident on a phase change erasable disk is less than 1 mW. With 10% to 30% reflected light and the available mark-to-space contrast on the disk, there is enough output signal to ensure greater than 50dB SNR. Generally there is also enough margin between read and write-erase power levels to allow some flexibility in the readout light level; for example, to increase the SNR without the danger of overwriting the disk.

MO readout relies on the Kerr effect, which changes the polarization of light from linear to elliptical, with the inducing of a 90° component upon reflection from recorded domains. The readout data is the 90° induced field component. The Kerr rotation in MO disk is of the order of one degree, i.e., the 90° component has very small amplitude. Thus, readout contrast is very low, much lower than for other types of erasable disks. To improve SNR, the readout incident intensity is increased by comparison to other erasable systems, but it cannot be higher than 3 to 5 mW in order to avoid erasing data. Unfortunately, because of feedback, laser noise increases by about 10 dB to 30 dB [20-25] from about -130 dBm/Hz for a BER of 10^{-12} to about -100 dBm/Hz relative RIN, when the laser operates at this power level. To maintain at least a ≥ 50 dB SNR in the SODR, the laser RIN should be below -130 dBm/Hz.

Laser feedback noise characteristics are summarized as follows: Reflected light from the MO disk and various optical interfaces is coupled back into the laser; the amount of back coupling or feedback is a function of both the magnitude and the phase (the location of the major reflecting surface) of the reflected light. Feedback causes the laser to oscillate in several modes, fluctuating between the modes, with energy transfer between them. Those fluctuations cause random coherence variations that result in intensity noise and phase noise in certain frequency ranges, depending upon the amount of feedback. At reflectance $\ll 1\%$, the noise consists of only low frequency spikes, presumably the result of mode hop between a small number of modes. At 1% to 10% reflectance, the noise is Gaussian-like, with a steady average value in the MHz range, i.e., in the baseband frequency range of the data. It increases to a maximum of about -110 to -100 dBm at power of 2 to 5 mW, decreases somewhat with increasing power, then increases again at higher power. At higher reflectance, the laser assumes one of two meta-stable modes, each with different noise characteristics.[26-27]

The concern with noise in MO systems is that not only the required readout intensity from the laser is about 3 to 5 mW, but also the reflectance into the laser is about 2 to 4%. This combination of laser output and the overall reflectance are both in the range of highest vulnerability to noise. As a result, MO systems suffer from laser wavelength stability and from increase RIN, which result in increased error rate in the data channel and increased timing errors in the servo channels. Thus, it is necessary to either reduce feedback or make it ineffective.

One obvious way to reduce feedback is through the use of optical isolators. Another way that is standard practice in single-diode commercial systems is to modulate the lasers light with high frequency rf when the system is in the readout mode. Other approaches to minimize feedback effects include the use of dual source techniques that optimize the write and read sources for their respective operations, or the use of wavelength stabilized sources, such as DFB or DBR lasers. We will evaluate each one of those techniques.

B. TECHNIQUES TO REDUCE FEEDBACK NOISE

1. High Frequency Modulation

High frequency modulation [28-33] consists of modulating the laser with an rf signal of frequency as high as possible, typically in the range of about 700 MHz. This process has the effect of broadening the laser line, hence, reducing coherence and related noise. Packaging laser diode arrays to carry such high frequency is difficult, the limitations being lead and relatively high diode capacitance. High speed modulation techniques require the use of strip line microwave technology for impedance matching, and the fabrication of diodes with low capacitance. This approach has not yet been sufficiently investigated in multi-diode systems.

2. Optical Isolators

The use of optical isolators may be more attractive than high-frequency modulation, but only if they can be packaged in special configuration. There exists commercial isolators that can provide up to 60 dB isolation. Until recently, they required long Faraday rotator crystals. For a 10-diode array with overall aperture of 1.35 mm and $9^\circ \times 30^\circ$ beam divergence, the optical isolator would be too bulky or would have a large enough numerical aperture to accommodate all the lasers. However, optical isolators, with such aperture, may eventually become feasible with the advent of bismuth-substituted gadolinium iron garnet [34-37]. This material has a very high Faraday rotation, about $4500^\circ/\text{cm}$. It is grown epitaxially, and its losses are relatively low at 830 nm. Since it can be grown in large area and can give a 45° rotation in about only 100 μm thickness, it can be used to make an optical isolator with large numerical aperture. Katayama and coworkers [38] have reported fabricating a two-diode array package incorporating an isolator in which this material is also the window in the hermetically sealed package for the diode array. Their data show a maximum reduction of RIN by 20 dB in the 3 to 10 mW power range and reflection in the 1 to 10% range. We believe that this approach using bi-substituted GaFe garnet is worth investigating for inclusion of a 10-diode array package for MO recording. An example of how a compact optical isolator can be used in a multi-element laser diode array is shown in Fig. V-1.

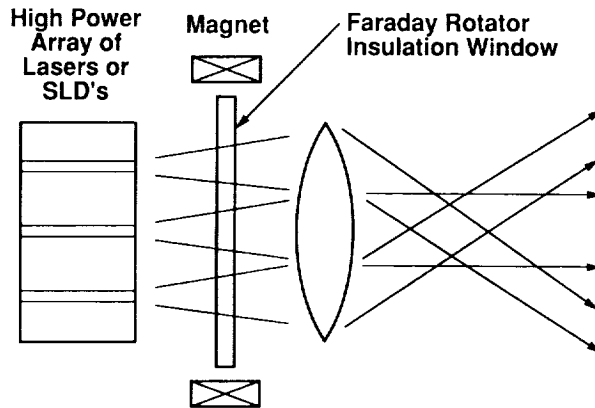


Figure V-1. Configuration of bismuth-substituted gadolinium iron garnet Faraday rotator as built-in isolator window for laser diode array.

3. Dual Source Techniques

Another method for avoiding feedback is to use dual sources with separate functions for reading and for writing-erasing. A dual source that is unaffected by feedback is the laser-SLD combination array shown in Fig. V-2.

It consists of a linear array in which the electrode pattern is configured into two parts. The front part is the emitting area with electrode pattern similar to any array described in this report. The back portion of the structure contains one single electrode that is common to all the diodes and can be connected to either a positive or a negative source. Let us call it the read-write-erase (RWE) control. This structure has the property, when the RWE electrode is set positive, together with the individually addressable electrodes, the full length of the cavity has optical gain and the structure acts as a high-power individually addressable laser diode array. This high-power configuration is used for writing and erasing where feedback and laser noise are of no consequence. When the RWE electrode is reverse biased, the whole back region of the array is lossy and absorbs the backward-directed light, resulting in no reflectance from that side of the structure. In this mode of operation, the structure cannot support Fabry-Perot modes, and it becomes an array of superluminescent diodes (SLDs), each emitting several milliwatts of power. The SLD [39] is a broadband source whose power can be made comparable to a laser and whose far-field is similar to the laser. It has several characteristics that make it suitable for reading out MO disks. The light

is polarized or can be made linearly polarized. Its optical bandwidth is equivalent to an electrical modulation of several thousand GHz without the use of rf. It inherently has lower RIN characteristics than a laser, and any feedback light injected in it is absorbed by the back attenuator. Figure V-3 shows the spectrum of a SLD, and Fig. V-4 shows the P-I characteristics and RIN of a laser and of a SLD made from the same wafer.[40] It clearly shows the increase of noise in a laser near threshold, even in the absence of feedback, and the essentially constant RIN of the SLD.

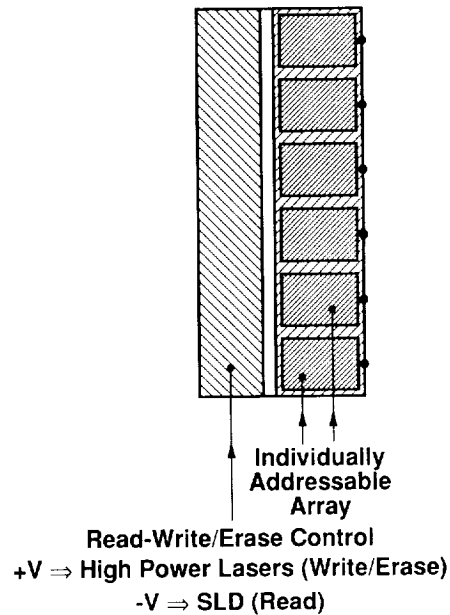


Figure V-2. Laser-superluminescent diode (SLD) array insensitive to feedback. When a positive voltage is applied to the large electrode at the left, the array functions as an array of high-power individually addressable laser diode array. When it is disconnected or reverse biased, the structure functions as an SLD array whose output is unaffected by feedback.

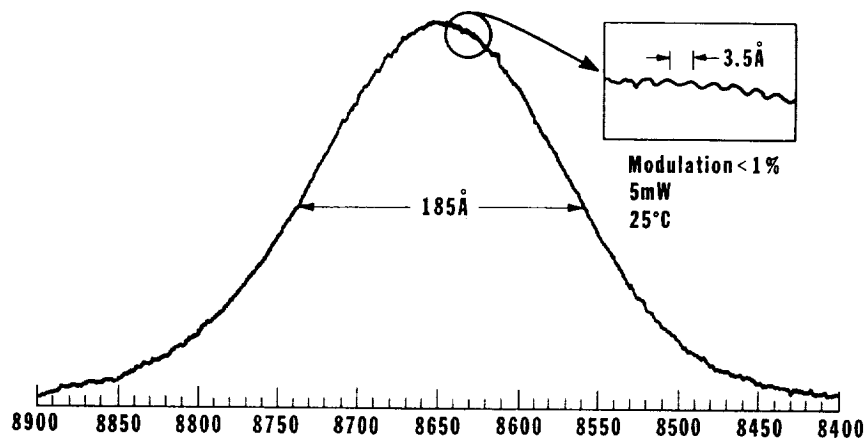


Figure V-3. Broadband spectrum of superluminescent diode.

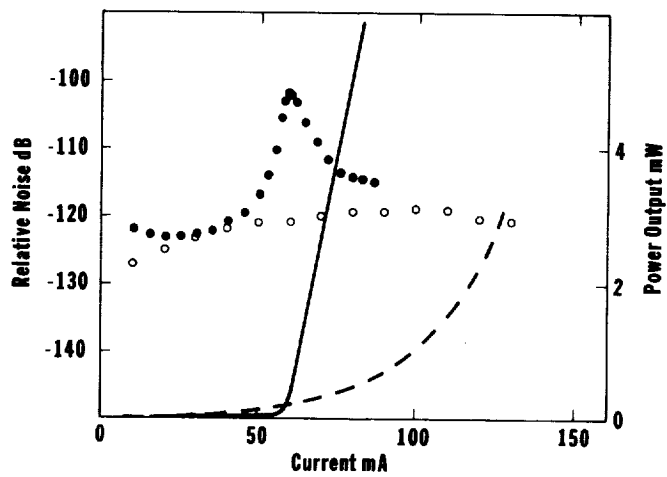


Figure V-4. Relative noise $20 \lg (dI/I)$ of SLD (open circle) and of a laser from the same wafer (black circles). Also shown is the P-I of a laser (solid line) and of SLD (dashed line).

An alternative source configuration for MO systems consists of physically separating the write-erase sources from the read sources, as shown in Fig. V-5. In this arrangement, an array of high power sources would be used for writing and erasing, with a polarizing beam splitter and quarter wave plate acting as an isolator. A separate array of polarized multibeam array would be used as a read source at lower power. The read sources can be combinations of any of the remedies described so far against feedback: DFB or DBR lasers, superluminescent diodes, lasers including thin Faraday rotator window, etc. A beam splitter is used to merge and separate the two optical paths. Additional optics (not shown in Fig. V-5) are used in the readout path for data detection.

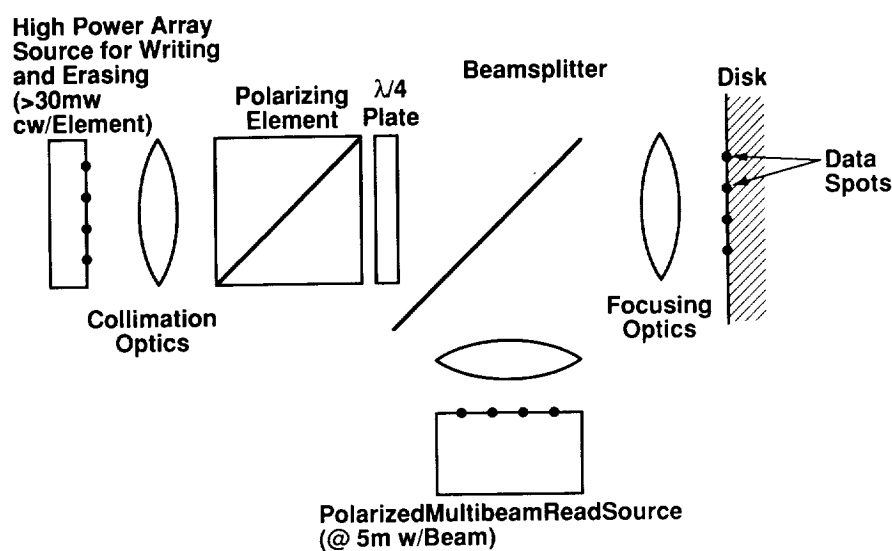


Figure V-5. Configuration using separate sources for write-erase and for read. The optics for write-erase sources contain a polarizing beam splitter and a quarter-wave plate to prevent feedback. The read sources are diodes, such as DFB or DBR lasers, SLDs, or lasers with built-in isolators. Readout detectors are not shown.

Figure V-6 shows yet another method of separating sources and functions, and one that provides additional capabilities as well. It consists of two, or more, linear independently addressable arrays of surface-emitting lasers arranged on a single chip as shown. The emitters are DBR types (to be discussed later in this report) with a first order grating used as feedback on one side of the gain region, and a second order grating on the other side to provide feedback as well as output coupling. This array can operate in many ways, and we present two of them as follows. In one mode, array 1 is used for write-erase, and array 2 for read. This mode provides separate source functions on a single chip. It also allows the

possibility of direct-read-after-write (DRAW). In another mode, array 1 is used for read-write erase array 2 is used as a back-up, to provide redundancy and extended systems life. The issues of redundancy and systems life have been given much consideration, without practical means of implementation. This two-dimensional array of GSE is the first practical approach; one that does not occupy excessive physical space, that can be remotely configured (from a ground station) or automatically reconfigured (from internally generated diagnostics data), and that is close to physical reality, as witnessed by progresses made to date at the David Sarnoff Research Center on GSE structures. Much more development of this technology is required, however, before it can be incorporated into real hardware.

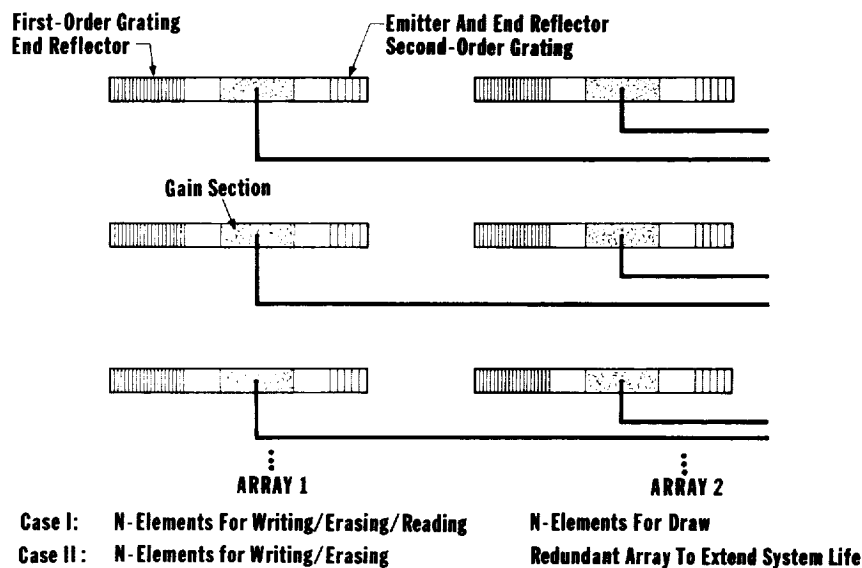


Figure V-6. Two-dimensional array that can be used either as a direct-read-after-write or as source with built-in redundancy.

4. Wavelength-Stabilized Sources: DFB/DBR Lasers

The use of optical isolators to reduce reflection would be sufficient if feedback were the only cause for laser mode hopping. Even without external feedback, Fabry-Perot (F-P) lasers are susceptible to mode hopping as a result of other factors, such as temperature variations, drive current, and aging. The spectral response of a F-P laser shows the possible lasing wavelengths is as shown in Fig. V-7. It is a set of lines with spacing $\Delta\lambda = \lambda^2/2n_eL$ within the laser gain spectrum, where λ is the free space wavelength of one of the resonances, n_e

and L are the cavity effective refractive index and length respectively. Lasing occurs at the wavelength that first meets the threshold condition:

$$r_1 r_2 e^{-j(\beta L + \phi)} = 1 \quad (V-1)$$

where $\beta = n_e k_0 + j \frac{1}{2} \bar{\alpha}$ is the complex propagation constant, $k_0 = 2\pi/\lambda$, and $\bar{\alpha}$ is the net gain coefficient, r_1 , and r_2 are the magnitudes of the front and back reflectances, and ϕ an arbitrary phase related to reflectance (from external surfaces).

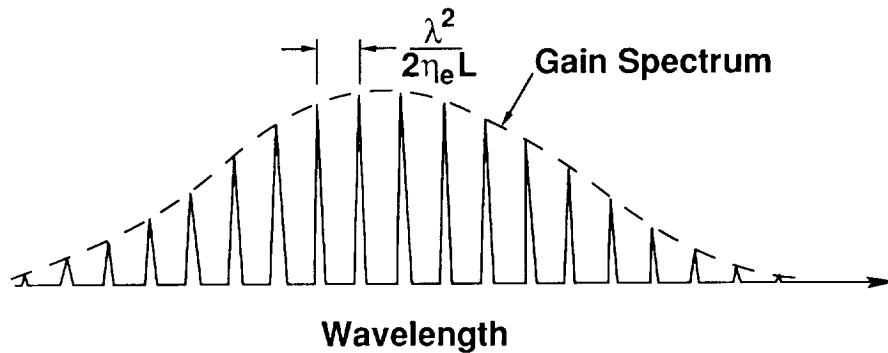


Figure V-7. Spectrum of Fabry-Perot laser near threshold.

In the absence of external feedback, ϕ is zero, r_1 and r_2 are the facet reflectances, and lasing occurs at the F-P wavelengths that satisfy Eq.(V-1) i.e., those for which $n_e k_0 L = m\pi$, where m is an integer, and when the reflectances and single pass gain are such that the $r_1 r_2 \exp(\bar{\alpha} L) = 1$. The effect of temperature, current, and age can vary the gain and phase, causing the output wavelength to hop between neighboring F-P modes. At low power, several F-P lines near the peak of the gain curve meet the threshold condition, and the laser output contains several longitudinal modes. At high power, the strongest line tends to saturate the gain and the laser may have stable operation in that one mode. In general, the higher the reflectance, the lower the required threshold gain.

In the presence of external feedback, the value of r_1 or r_2 changes and together with the additional phase factor ϕ , they change the threshold condition. ϕ depends upon the location of the main reflecting surface and upon its surface characteristics. Lasing will occur at any new value of the parameters that satisfy

(V-1). Thus, external feedback introduces wavelength instabilities and the consequent increase of RIN as described earlier.

It is therefore necessary to develop wavelength stabilized laser arrays, i.e., single-mode lasers that are free from feedback and related noise. Such means exist in DFB and DBR lasers, as will be described in the next section.

Section VI

ANALYSIS OF DFB AND DBR LASER SOURCES FOR MAGNETO-OPTIC RECORDING

The structures for DFB and DBR lasers are shown schematically in Fig. VI-1a and Fig. VI-1b respectively.

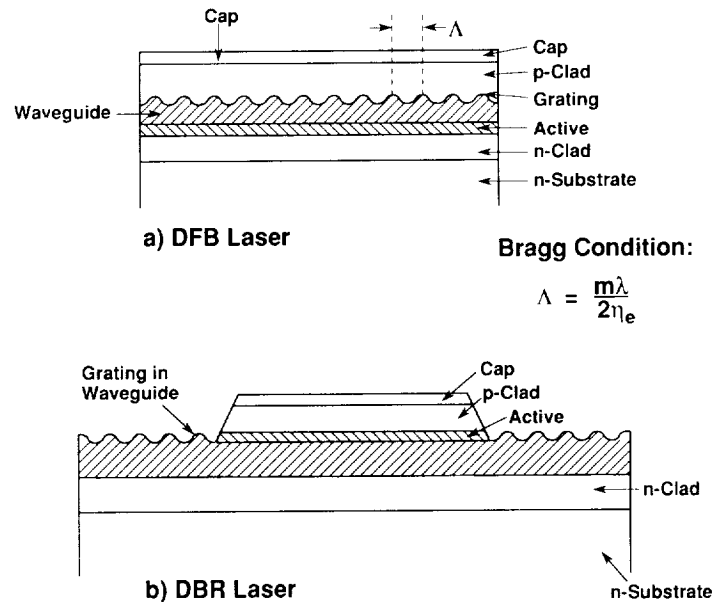


Figure VI-1. (a) Structure of DFB laser. The grating is along the active region. (b) Structure of DBR laser. The gratings are placed in passive regions at the ends of the active region. They serve mainly as wavelength selective reflectors.

In the DFB laser, the grating is placed in a waveguide layer above (or below) the active layer. It interacts with the optical field in the active region, through the evanescent field in the waveguide, causing reflection of both forward and backward waves. In the DBR laser, the grating is placed in passive waveguides in the end region, with the purpose of providing reflection feedback into the active region. Its function is thus similar to the facet in the F-P laser, except that the reflection is wavelength selective.

In this section, we report on the investigation of design and implementation strategies that lead to a choice between the two types of devices as sources for MO disk systems. For MO applications, the features of interest in a laser are:

- Stable operation at one wavelength
- Immunity to mode hop
- Low RIN
- High power operation (30 mW) for write and erase
- Long life, i.e., the avoidance of degradation mechanisms that may affect device life. The features of both types of lasers will be examined in order to determine which one is better suited to MO systems.

A. DFB LASERS

1. Modal Analysis

The operation of DFB lasers is readily derived from the theory of wave propagation in periodic structures. The grating introduces a periodic component in the permittivity of the waveguiding region. According to the Floquet-Block theorem for periodic differential equations, the wave propagating in the structure is also periodic, with the periodicity of the structure. A Fourier expansion decomposes it into a sum of its "partial" waves (harmonics). Pairs of these partial waves have matching phase in so-called "Bragg regions" where the grating period Λ and the optical wavelength λ are related by:

$$\Lambda = \frac{m\lambda_B}{2n_e} \quad (\text{VI-2})$$

where m is an integer, and where the subscript B is added to identify the Bragg interaction. It is well known that energy exchange (or coupling) occurs between waves having matching phase, and in the case of the DFB laser, it occurs between a forward and backward wave harmonic.

Kogelnick and Shank [44] have used coupled-mode theory to derive the propagating modes and their threshold conditions in DFB structures. In a uniform waveguide, the wave amplitudes are constant with respect to longitudinal position z except for an attenuation factor if the guide is lossy. In the presence of a dielectric perturbation $\Delta\epsilon$, they become z -dependent, and if they are slowly varying, they are well described by coupled-mode theory. Near the Bragg region, the electric field, assumed to be polarized in the x direction and propagating in the z direction, is given by:

$$E(x,y,z) = u(x,y) [A(z)\exp(-j\beta_0 z) + B(z)\exp(j\beta_0 z)] \quad (\text{VI-3})$$

where $u(x,y)$ is the mode function (determined by guide geometry), where $\beta_0 = m\pi/\Lambda$ is the Bragg wavenumber, and where $A(z)$ and $B(z)$ are the coupled waves. It should be noted that Eq. VI-3 is merely a representation of the field near the Bragg region. β_0 is not the propagating wavenumber. The propagating wavenumber q is contained in the expressions for $A(z)$, and $B(z)$ which are given by:

$$A(z) = A_1 \exp(-jqz) + r(q)B_2 \exp(jqz), \quad (\text{VI-4})$$

$$B(z) = r(q)A_1 \exp(-jqz) + B_2 \exp(jqz)$$

where A_1 and B_2 are constants, and $r(q)$ is the DFB reflection coefficient, and where $A(z)$ and $B(z)$ obey the following coupled-mode equations:

$$\frac{dA}{dz} = -j\Delta\beta A - j\kappa B \quad (\text{VI-5})$$

$$-\frac{dB}{dz} = j\Delta\beta B - j\kappa A$$

In the above expressions, $\Delta\beta = \beta - \beta_0$ is the phase mismatch, and where β is the complex propagation constant in the absence of the grating. β is given by:

$$\beta = n_e k_0 + j \frac{1}{2} \bar{\alpha} \quad (\text{VI-6})$$

as described earlier, and the coupling coefficient is given by:

$$\kappa = \frac{k_0^2}{2\beta} \frac{\int_{-\infty}^{\infty} \Delta\epsilon u^2(x,y) dx dy}{\int_{-\infty}^{\infty} u^2(x,y) dx dy} \quad (\text{VI-7})$$

The propagation constant q obeys the dispersion relation

$$q = \pm[(\Delta\beta)^2 - \kappa^2]^{1/2} \quad (\text{VI-8})$$

and the DFB reflection coefficient $r(q)$ is given by $r(q)$ is given by:

$$r(q) = -\frac{\kappa}{q + \Delta\beta} \quad (\text{VI-9})$$

The above treatment applies to a structure of infinite length, and expression VI-8 gives the propagation constant. The waves propagate undisturbed as long as q is positive real. However, for $(\Delta\beta)^2 < \kappa^2$, q is pure imaginary and there is no propagation, i.e., there is a stop band of half-width equal to κ centered at the Bragg wavenumbers. The longitudinal mode spectral and the threshold condition for the various modes are obtained when the finite length of the structure is taken into consideration.

2. Threshold condition

For an infinitely long structure, q can have arbitrary values. For a finite length structure, the boundary conditions can be satisfied at only discrete values of q . For any value of q satisfying the boundary conditions to yield an output light with no input light, the real part of q gives the longitudinal mode frequency, and its imaginary part gives the threshold gain. The DFB will lase at the frequency corresponding to the mode for which the threshold gain is the lowest. Then, if there is enough mode discrimination, only the mode with the lowest threshold will be favored for lasing.

For a finite length DFB, the effective facet reflectance is complex and its phase may be arbitrary, since the facet occurs at some arbitrary point in the grating. In general, they are given by:

$$\begin{aligned} r_1 &= R_1^{1/2} \exp(-j\phi_1) \\ r_2 &= R_2^{1/2} \exp(-j\phi_2) \end{aligned} \quad (\text{VI-10})$$

and the boundary conditions are, for a DFB of length L ,

$$A(0) = r_1 B(0) \tag{VI-11}$$

$$B(L) = r_2 A(L)$$

Equations VI-4 with boundary conditions (VI-11) have a non-trivial solution only if the determinant of the coefficients vanishes, i.e., if the following resonance condition is satisfied.

$$\left(\frac{r_1 - r}{1 - rr_1}\right) \left(\frac{r_2 - r}{1 - rr_2}\right) \exp(-2jqL) = 1 \tag{VI-12}$$

Equation VI-12 is the DFB laser eigenvalue equation and its numerical solution gives the longitudinal modes and their thresholds. Various effects can be achieved by appropriate choices of r_1 , r_2 , and r (or κ). We note that this equation is reduced to the F-P threshold condition, $r_1 r_2 \exp(-2jqL) = 1$, if the coupling coefficient is zero, i.e., in the absence of the grating ($\kappa = 0$). Without going into mathematical details, we summarize the important results below when κ is non-zero.

In the case of pure DFB operation, the facet reflections r_1 and r_2 are zero. Eq. VI-1-12 gives $r^2 \exp(-2jqL) = 1$, which, together with (VI 1-9) gives;

$$\kappa \sin qL = \pm jq \tag{VI-13}$$

Equation VI-13 can be solved graphically. The resulting DFB modes and their threshold gains are shown in Fig. VI-2a. As expected, there is no propagating wave at the Bragg frequency. There are several modes symmetrically placed with respect to the Bragg frequency. The two modes closest to the Bragg frequency (heavy lines) have the lowest but equal threshold gain. Therefore the simple DFB laser with zero facet reflectance will lase in those two modes. Unlike the F-P laser for which the treshold gain is almost the same for a large number of modes, the DFB has a much higher threshold requirement for the modes that are further away from the Bragg frequency, and therefore, it has high selectivity. However, the existence of two modes is not desirable, and some means must be found to remove the degeneracy (remove one of the lasing modes).

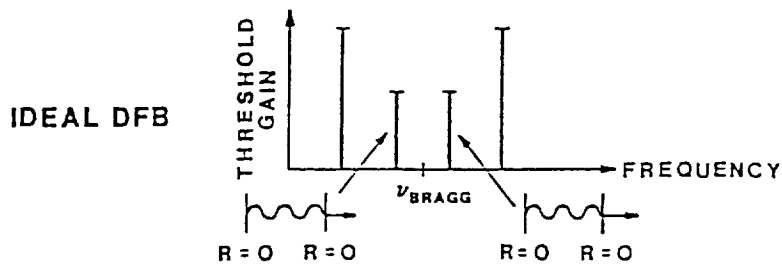


Figure VI-2a. Ideal DFB has two modes with lowest threshold, identified by arrows.

One method consists of shifting the gain curve with respect to the DFB spectrum in order to give a lower threshold to one of the modes, as indicated in Fig. VI-2b (the arrow points to be the selected line). This is not a desirable approach because the gain curve can vary with current, temperature, and age. Furthermore, it is very broad (about 150\AA at the 3dB point for AlGaAs lasers), and therefore, this approach is unstable, and does not provide enough selectivity.

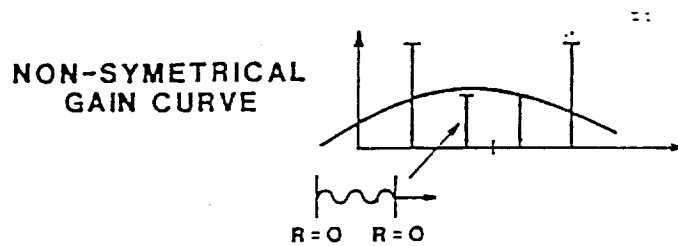


Figure VI-2b. Shifting gain curve to select one mode.

Another method is to provide radiation losses for one of the degenerate modes. For example, if the grating is a second order grating $m = 2$ in Eq. VI-2 instead of a first order grating, energy will be radiated out of the plane of the grating. Henry and Kazarinov have shown [42] that this loss is not the same for the modes on the two sides of the Bragg resonance, and hence, one of the modes will have a lower threshold, as shown in Fig. IV-2c.

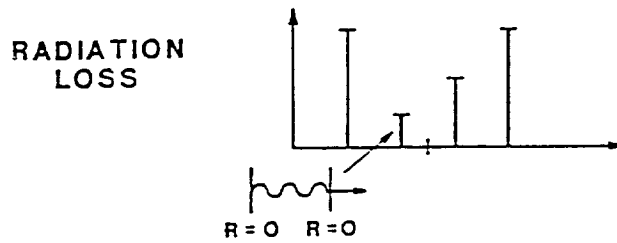


Figure VI-2c. Use of radiation loss to select single mode.

Two other methods are shown for removing the DFB degeneracy, and their significance lies in the fact that they introduce a low gain threshold mode referred to as "gap mode", at the Bragg frequency itself. The first method is the introduction of a half-period (quarter wave) shift somewhere in the grating. This breaks the grating uniformity and introduces the equivalent of a half wavelength cavity that is resonant at the Bragg frequency. The effect of this scheme is to introduce a low threshold mode at the Bragg frequency. This type of structure is called the Quarter-Wave-Shifted (QWS) DFB laser. The second method is obtained from non-symmetrical facet reflection. It can be shown that if one of the facets has near unity reflectance and the other has near zero reflectance, a gap mode is also introduced in the spectrum. This structure is equivalent (as far as the modes are concerned) to a DFB with uncoated facets that is twice as long, and that has a shift in grating periodicity. In the case of a facet-coated DFB, the facet reflection will act as a grating phase shift, with the magnitude of the shift dependent on the position of the facet with respect to the grating. The gap mode in the DFB spectrum is shown in Fig. VI-2d.

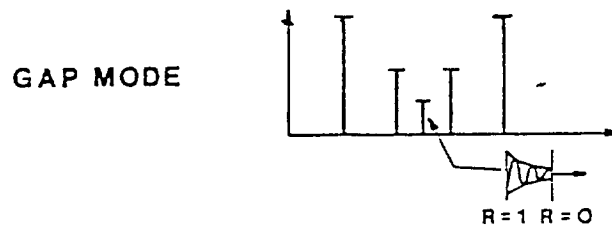


Figure VI-2d. Creating low threshold "gap mode" at the Bragg wavelength.

The stronger the coupling coefficient κ is, the lower is the required gain threshold. Figure VI-3 shows the relation between the threshold gain coefficient and the coupling coefficient.

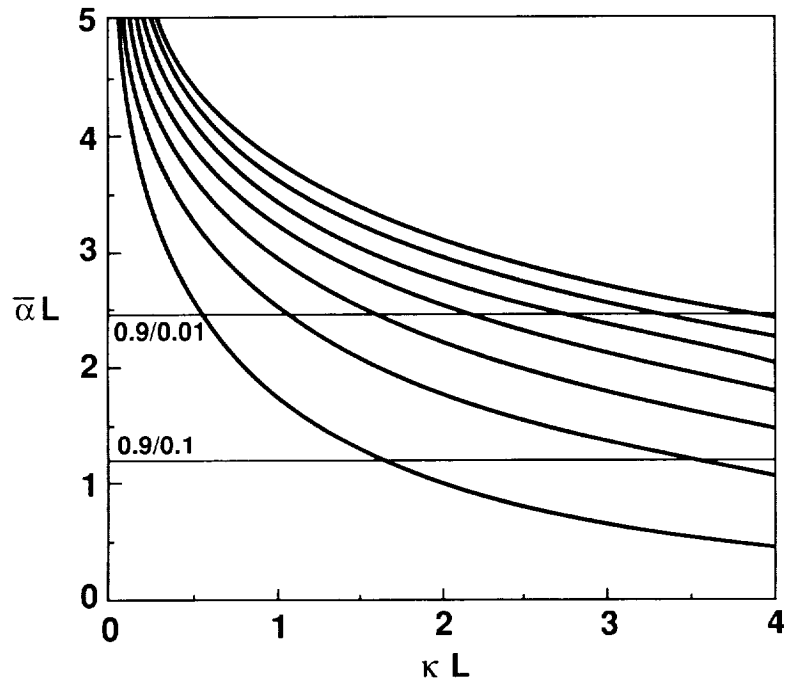


Figure VI-3. Relation of threshold gain to coupling coefficient for DFB lasers.

It is therefore advantageous to have as strong a coupling coefficient as possible, but up to a certain point. However, if the grating is too strong, the spatial distribution of the modes becomes very non-uniform along the direction of propagation. This can result in multimode operation due to spatial hole burning. The coupling strength is a function of the grating corrugation depth, and a plot is given for a triangular grating in Fig. VI-4.

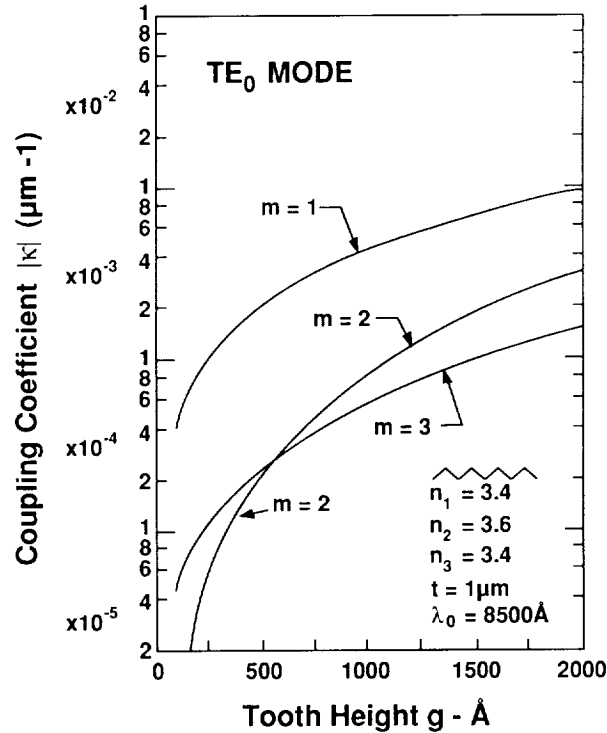


Figure VI-4. Plot of coupling coefficient for triangular grating in DFB lasers.

B. DBR LASERS

In the DBR laser, the gain region is separated from the grating regions. The gratings are in passive wave guides at the ends of the device, and their purpose is to provide frequency selective reflectance as opposed to the broad-band facet reflectance of the F-P laser. The analysis of the grating reflection is also given by coupled-mode theory, and the general solution is the same as Eq. VI-4. If we denote the reflectance of the grating, referenced to the junction between the gain region and the grating by r_g , the threshold condition is given, for identical gratings, by

$$r_g^2 \exp(-j2\beta L) = 1 \quad (\text{VI-14})$$

where β is the same as before. If there are no transition discontinuity (between gain region and grating) or facet reflection, then r_g is given by

$$r_g = \frac{j k \sin(qL_g)}{q \cos(qL_g) + j \Delta \beta_g \sin(qL_g)} \quad (\text{VI-15})$$

where $\Delta \beta_g = \delta - j \frac{1}{2} \alpha_g$, and where α_g , is the grating power absorption coefficient.

DBR lasers do not have a stop band at the Bragg frequency. In fact, under ideal conditions, the mode of lowest gain threshold should occur at the Bragg frequency itself because this is where r_g has its highest magnitude. However, because the feedback is not distributed within the gain region, the mode spectrum and oscillation conditions can vary, and they are significantly different than for a DFB laser. The mode frequencies are obtained by setting the phase of the left-hand side of Eq. VI-14 to an integer multiple of 2π . Once these eigen-frequencies are found, the required threshold gain is determined by setting to unity the amplitude of the left-hand side of Eq. VI-14. It is thus clear that the actual wavelength of operation is critically sensitive to the phase length of the gain region. As operating conditions change (e.g. current, temperature), the wavelength of the various modes with respect to the Bragg resonance will change. Thus, it is possible that at one set of operating conditions one mode will be closest to the Bragg condition and will be favored to lase; if the conditions are changed, another mode will be favored. Therefore mode hopping is possible. However, despite this possibility for mode hopping, DBR lasers have been demonstrated to operate without mode hopping at output powers of several tens of milliwatts and over temperature variations of 50 to 70 °C.

C. CHOICE BETWEEN DFB AND DBR STRUCTURES

DBR lasers have the advantage that growth is not required over the grating region. It is well suited for optical integration because the grating can be designed to be both an output coupler and a coupling element to other devices, as in the GSE arrays under development at the David Sarnoff Research Center. With the addition of a long external cavity, it is an excellent structure for low chirp narrow linewidth sources. However, it has the disadvantage that mode stability and selectivity depend on the phase length of the active region, on the length of the grating regions, and on the magnitude and phase of facet reflection. Furthermore, the transition between the active and grating regions may introduce significant radiation loss, which causes the lasing threshold to increase. Special waveguide transition is required to overcome radiation loss.

On the other hand, DFB lasers are real optical resonators that can have single mode operation over wide operating ranges. There is no waveguide transition to design, and the introduction of the QW shift, high facet reflectance on one side or longitudinal waveguide width variations can force the device to lase at exactly the Bragg wavelength with high selectivity and low threshold, regardless of operating conditions. This Bragg wavelength is determined strictly by the grating period and the waveguide's effective refractive index, which are constant. In early DFB lasers, the grating was made in the active layer, and regrowth was required over that layer. Poor regrowth caused problems with device life, due to the introduction of non-radiative recombination centers. Later, the separate confinement structures solved the problem, because it allowed the fabrication of the grating in the confinement layer, which already protects the active layer. Finally TE/TM mode selectivity can be accomplished by facet reflection or, more importantly, by the use of QW active layers. For MO recording systems, long life, high power, stable single mode operation, with low possibility of mode variations or hopping, are required. We conclude that DFB lasers are the most suitable type of stable source for MO operation.

D. DESIGN FOR OPTICAL RECORDING: FIRST ORDER VS SECOND ORDER GRATING

Having shown that the DFB laser is suitable as a mode-stabilized source for optical recording, we now examine the several issues that are involved in the design of such a source. The first issue is the laser geometry to be considered for inclusion of the DFB grating, with the condition that high power and low RIN are required in addition to modal stability. Since the active layer must be protected from the steps required to make the grating and regrow over it, the grating must be placed in a layer that functions both as a protective layer for the active layer and as a waveguide in which to place the grating. Therefore, a structure with separate confinement layers is desired. It can be a single QW, double QW, or even a double heterostructure with "thin" (400Å to 600 Å) active layer. The QW structures offer the advantage of giving control on the TE/TM polarization in favor of the TE mode. The structure must also provide adequate means for current and optical confinements. In that respect, gain-guided structures, are not desirable. Preferred structures are index-guided structures such as the ridge, buried ridge, and I-CSP configurations. The I-CSP DFB laser is an interesting choice because

it provides the high power capability of the CSP without the alignment problems encountered in ordinary CSP lasers, due to its self-aligned geometry. It is also known to provide stable lateral guiding and high confinement characteristics. However, it does require an extra growth step, compared to the buried ridge structure.

The other important issue relates to the type of grating to be used. Fabrication of the grating should have a reasonable yield and should lend itself to inspection prior to regrowth. In addition, the grating design should facilitate mode selection, preferably by using a quarter-wave shift or a shift by reflection from the back facet. The grating is typically made by holographic exposure, using the 3511Å line of an argon laser on a photoresist layer spun on the wafer. The photoresist is then developed and the exposed lines are chemically etched. Depending on the orientation of the grating lines, with respect to the crystal planes, two distinct grating shapes can be formed. If the grooves are aligned with respect to the (011) direction, a dovetail groove shape is obtained, and if the lines are aligned with respect to the $[0\bar{1}1]$ direction, a V-groove shape is obtained. Etching is carried both laterally and vertically. If it is allowed to proceed to completion, a triangular-shaped groove is obtained. If the etching is not complete, the shape of the groove is trapezoidal.

The simplest DFB structure is one that produces the Bragg condition in the first order ($m = 1$ in Eq. VI-2), with the grating period equal to half wavelength in the guide. For a 8300 Å laser with a AlGaAs waveguide having a refractive index of 3.4, the grating period is 1220 Å. Such a grating is very difficult to fabricate and, it cannot be inspected with visible light. Furthermore, the grating depth, hence, the DFB coupling coefficient, cannot be easily controlled. The fabrication difficulty is enhanced by the fact that a quarter-wave shift may be desired in order to operate at the Bragg wavelength for single mode performance.

Several methods have been used or proposed to fabricate gratings of period in the 1000 Å range in III-V compounds. The most feasible method appears to be the "divide-by-two", and we describe three of these here. The first method is illustrated in Fig. VI-5. A grating of period equal to twice the desired period is fabricated on the substrate using conventional holographic and photoresist techniques, then it is covered with a dielectric, such as silicon nitride, as shown in Fig. VI-5a. The dielectric is ion milled to expose the grating crests, as shown in Fig. VI-5b, and a second grating with the same period is fabricated on the

material with a half-period shift as shown in Fig. VI-5c. The shift can be obtained either by inserting a half-wave plate in one of the holographic beams, or by mounting one of the mirrors on a PZT element to which a voltage is applied to create a half-wave displacement. The final grating is obtained after removal of the residual dielectric.

A second method is shown in Fig. VI-6. According to this technique, the first grating is exposed as before, as shown in Fig. VI-6a, but it is not etched. Instead, it is covered with a nitride film (Fig. VI-6b) on which a second holographic exposure is done, as shown in Fig. VI-6c. The dual pattern is then etched to produce the desired grating (Fig. VI-6d).

A third method for the divide-by-two approach is shown in Fig. VI-7. In this case, a rectangular grating is formed in the resist, and a conformal dielectric coating is deposited, as shown in Fig. VI-7b. This is followed by an ion beam etch at grazing incidence to expose the top of the photoresist as shown in Fig. VI-7c. The resist is then dissolved (Fig. VI-7d) and the substrate is ion beam etched (Fig. VI-7e). The finished grating is obtained after removal of the residual oxide mask (Fig. VI-7f).

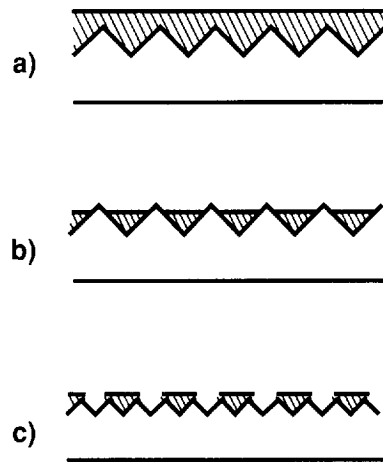
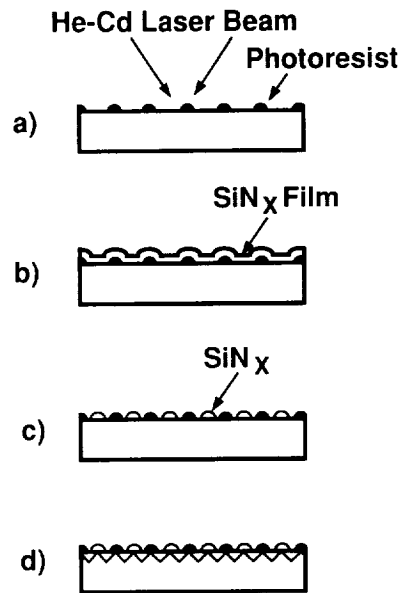


Figure VI-5. A "divide-by-two" method to produce grating with period in the 1000Å range.



Fabrication steps of 120 nm period grating.

- a. Holographic exposure
- b. SiN_x deposition by ECR-CVD
- c. Etch SiN_x with BHF
- d. Etch substrate

Figure VI-6. Alternative method to produce short period gratings (details in text).

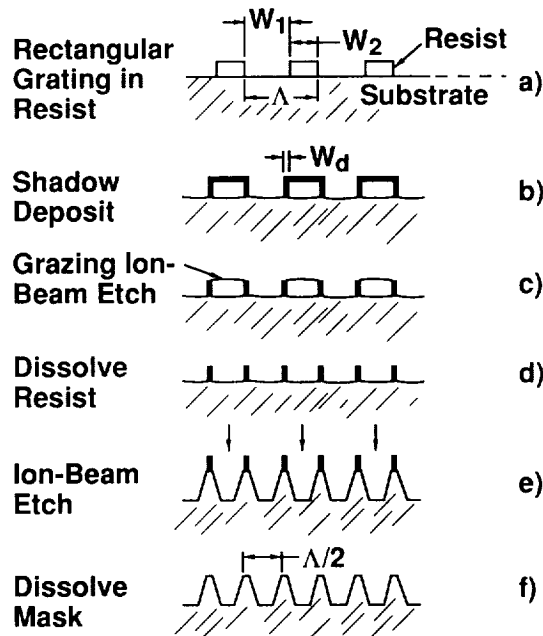


Figure VI-7. Third method for producing short period gratings.

The other techniques used for making high-pitch gratings include direct E-beam writing, the use of short wavelength lasers, the use of high index prisms, immersion in high index fluid, the use of cross gratings, and the use of focussed ion beam etching. These methods and their relative merits are summarized in Table VI-1.

Table VI-1
Grating Fabrication Methods For $\Lambda \sim 1000\text{\AA}$

CONCEPT	MIN	COMMENTS
1. DIVIDE BY 2	~878 \AA (Ar) ~813 \AA (HeCd)	QUESTIONABLE REPRODUCIBILITY
2. E-BEAM WRITING	~1000 \AA	~1 mm x 1 mm FIELD; TIME CONSUMING 1/4-WAVE SHIFT EASY, \$1000 K
3. SHORT WAVELENGTH LASERS		
- XENON	$\lambda = 2315 \text{\AA}$	~1 mm x 1 mm FIELD; NON-COMMERCIAL LASER COHERENCE? FIELD? PMMA, \$60K; PULSED
- ArF,	$\lambda = 965 \text{\AA}$	
4. HIGH INDEX PRISM n ~ 1.7	~1157 \AA (Ar) ~1161 \AA (HeCd)	REQUIRES PLANAR WAFER; \$5K
5. IMMERSION IN HIGH INDEX FLUID n ~ 1.4	~1254 \AA (Ar)	FLUID COMPATIBILITY; > 1000 \AA , \$10K
6. CROSS GRATING	< 1000 \AA	LATERAL SCATTERING; EXISTING CAPABILITY
7. FOCUSED ION BEAM ETCHING	~ 1000 \AA	NOT DEMONSTRATED; \$500 K 140 μM X 140 μM FIELD 1/4 WAVE SHIFT EASY

As can be seen from the above discussion, the fabrication of a first order sinusoidal grating for a 830 nm DFB laser (grating period of 1200 \AA) is not an easy task. However, a non-sinusoidal grating can be designed to have a strong harmonic component in any specific order. For example, a grating can be designed to have a fundamental wavelength of 2400 \AA with a strong component at 1200 \AA (second harmonic). Such a grating, designed to operate at the second harmonic is called a "second order" grating, and a DFB laser containing it would have a strong response at the second Bragg condition, i.e., the condition

corresponding to $m = 2$ in Eq.VI-2. It is also easier to fabricate than a "first order" grating, i.e., one for which $m = 1$, because the grating spacing is twice as large as that for the first order grating. The second order grating is also desirable because it can be used to enhance mode selection. The basic idea here is to use available techniques of holography and chemical photolithography, perhaps enhanced by ion beam etching to create a non-sinusoidal grating of suitable shape to enhance the second harmonic. Figure VI-8 illustrates some grating shapes that are suitable for second order coupling and others that are not. The rectangular grating can be made to have a relatively strong second harmonic component.

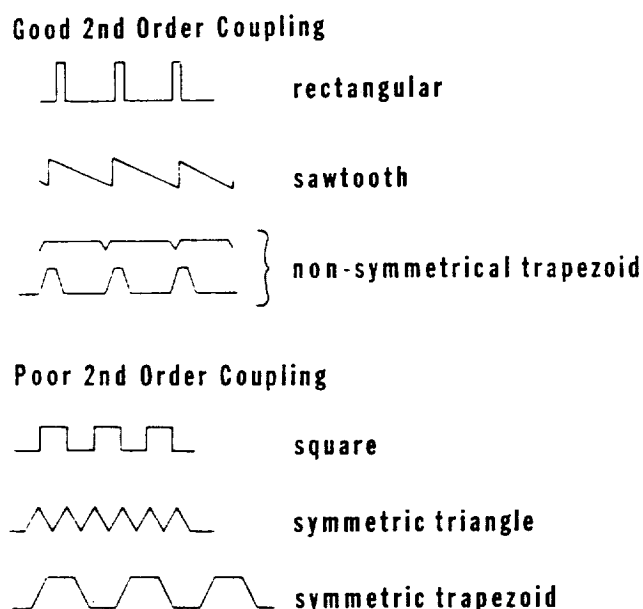


Figure VI-8. Grating shape categorized as good and poor for second order DFB laser.

Since the coupling coefficient is proportional to the amplitude of the respective component of waveguide permittivity perturbation, the magnitude of the grating's second harmonic Fourier coefficient is thus a measure of the coupling coefficient in that order. The second order coupling strength of several gratings is given in Table VI-2.

Table VI-2
COMPARISON OF 1ST AND 2ND BRAGG REFLECTORS

<u>Grating Shape</u>	<u>Order</u>	<u>Relative κ</u>
Sinusoidal	1	1
sinusoidal	2	0.01 to 0.1
Rectangular (25% d.c.)	2	0.6
Sawtooth	2	0.3
Triangular	2	0.01 to 0.1
half-sine	2	0.4

We see that a rectangular grating with 25% duty factor has a second order coupling strength of 60% of the first order coupling strength. It can be made by a combination of chemical and ion beam etchings. The above analysis concludes our preliminary study of DFB and DBR lasers for optical recording array sources. Several options have been examined and our preferred choices are described. We recommend the fabrication of DFB arrays using a second order grating embedded in the confinement layer above the active layer, in an index-guided structure, such as the I-CSP, that provide both current and optical confinement.

Section VII

CONCLUSION

We have continued development of monolithic arrays of individually addressable AlGaAs CSP laser diodes for use as the source of light in high data rate multichannel optical data storage systems. The design of high-power CSP lasers with linear light vs current characteristics depends critically on several design parameters, such as the thickness of the n-confinement layer, the width of the V-groove, and the width and alignment of the zinc diffusion stripe. Improvements to the design and a better understanding of the critical device and processing parameters, have led to the fabrication, testing, and delivery of ten-diode arrays having output power exceeding 30 mW cw, with linear light-vs-current characteristics and single longitudinal mode spectral characteristics.

The limitations of CSP structures were examined, and the inverse CSP (ICSP) structure, grown by metalorganic chemical vapor deposition technique (MOCVD), was suggested as a structure that could be fabricated more reproducibly, and with better performance than the CSP. Preliminary results on quantum well ICSP arrays indicate that this structure lead to threshold currents of 12 to 15 mA, as compared to 40-60 mA for CSPs.

We have explored the impact of systems response and requirements on laser design. In particular, we have assessed the effect of feedback on the laser sources, with emphasis on its effect on mode stability and the consequent increase of relative intensity noise (RIN). This increase in RIN degrades systems performance, in the sense that it increases bit error rate and introduces systems timing errors. We examined several alternative techniques, both in systems design and laser structure, to reduce feedback or minimize its effect on systems performance. They include the use of high frequency modulation, optical isolators, dual source technoques, and wavelength-stabilized sources. From the viewpoint of laser design, we show that structures having frequency selective feedback, such as DFB and DBR structures, provide the desired longitudinal modes stability. Finally, we presented an analysis DFB and DBR lasers and fabrication considerations leading to the choice of DFB lasers as suitable for magneto-optic recording systems.

The accomplishment of this work include:

- The complete evaluation and understanding of the CSP approach
- Improvement of processing techniques leading to the fabrication of deliverable arrays
- The demonstration of new arrays grown by MOCVD having threshold current less than one-half the threshold current of LPE arrays
- The demonstration of machine-assisted bonding technique suitable for space application
- The description of DFB laser structures for use in high-power optical recording applications

Section VIII

REFERENCES

1. B. Hill, "Some Aspects of a Large Capacity Holographic Memory," *Appl. Opt.* 11, 1, 182, Jan. 1972.
2. A. Vander Lugt, "Design Relationships for Holographic Memories," *Appl. Opt.* 12, 7, 1675, July 1973.
3. H. Kiemle, "Considerations on Holographic Memories in the Gigabyte Region," *Appl. Opt.* 13, 4, 803, April 1974.
4. A. Vander Lugt, "Packing Density in Holographic Systems," *Appl. Opt.* 14, 15, 1061, May 1975.
5. T.K. Gaylord, "Memories, Optical Holographic," *The Optical Industry and Systems Purchasing Directory*, p.E-116, 1982.
6. R.A. Bartolini, "Optical Recording: High-Density Information Storage and Retrieval," *Proc. IEEE*, 70, 6, 589, 1982.
7. SPIE Proceedings "Optical Mass Data Storage II," 18-22 Aug. 1986, San Diego, CA, and others.
8. D.B. Carlin, J.P. Bednarz, C.J. Kaiser, J.C. Connolly, and M.G. Harvey, "Multi-channel Optical Recording Using Monolithic Arrays of Diode Lasers," *Appl. Optics* 23, 3994 (15 November 1984).
9. Technical Digest, "Optical Data Storage," Topical Meeting on Optical Data Storage, Incline Village, Nevada, Jan. 17-20, 1983.
10. Technical Digest, "International Symposium on Optical Memory," 1989 (ISOM'90) Kobe, Japan, Sept. 26-28, 1989.
11. K. Aiki, M. Nakamura, T. Kuroda, J. Umeda, R. Ito, Naoki Chinone, and M. Maeda, "Transverse mode stabilized $\text{Al}_x\text{Ga}_{1-x}\text{As}$ injection lasers with channeled-substrate-planar structure," *IEEE Journal of Quantum Electronics* QE-14 (2), 89-94 (1978).

12. S. Yamamoto, H. Hayashi, S. Yano, T. Sakurai, and T. Hijikata, "Visible GaAlAs V-channeled substrate inner stripe laser with stabilized mode using p-GaAs substrate," *Appl. Phys. Lett.* 40 (5), 372-374 (1982).
13. B. Goldstein, M. Ettenberg, N.A. Dinkel, and J.K. Butler, "A high-power channeled-substrate-planar AlGaAs laser," *Appl. Phys. Lett.* 47, 655-657 (1985).
14. T. Kuroda, M. Nakamura, K. Aiki, and J. Umeda, "Channeled-substrate-planar-structure $\text{Al}_x\text{Ga}_{1-x}\text{As}$ lasers: an analytical waveguide study," *Applied Optics*, 17 (20), 3264-3267 (1978).
15. S. Wang, C. Chen, A.S. Liao, and L. Figueroa, "Control of mode behavior in semiconductor lasers," *IEEE Journal of Quantum Electron.* QE-17 (4), 453-468 (1981).
16. J.K. Butler, G.A. Evans, B. Goldstein, "Analysis and performance of channeled-substrate-planar double-heterojunction lasers with geometrical asymmetries," *IEEE J. Quan. Electron.* QE-23 (11) 1890-1899 (1987).
17. G.A. Evans, B. Goldstein, and J.K. Butler, "Observations and consequences of non-uniform aluminum concentrations in the channel regions of AlGaAs channeled-substrate-planar lasers," *IEEE J. Quan. Electron.* QE-23 (11), 1900-1908 (1987).
18. J.J. Hsieh, "Thickness and surface morphology of GaAs LPE layers grown by supercooling, step-cooling, equilibrium-cooling, and two-phase solution techniques," *J. Crystal Growth* 27, 49 (1974).
19. W. Nakwaski, "Thermal properties of buried heterostructure laser diodes, *IEE Proceedings* Vol. 134, No. 1, Feb. 1987, pp 87-94.
20. R. Lang and K. Kobayashi, "External Optical Feedback Effects on Semiconductor Injection Laser Properties," *IEEE J. Quantum Electron.* QE-16, 347 (1980).
21. N. Chinone, T. Takahashi, T. Kajimura, and M. Ojima, "Low Frequency Mode-Hopping Noise of Index-Guided Semiconductor for Lasers," in *Proceedings, Eighth Semiconductor Laser Conference* No. 25 (IEEE, New York, 1982).

22. A. Arimoto and M. Ojima, "Diode Laser Noise at Control Frequencies in Optical Videodisc Players," *Appl. Opt.* 23, 2913 (1984).
23. J. Biersterbos, A. Beef, W. Linders, and G. Acket, "Low Frequency Mode Hopping Optical Noise in GaAlAs Channeled Substrate Lasers Induced by Optical Feedback, *IEEE J. Quantum Electron.* QE-19, 986 (1983).
24. G. Arnold and K. Petermann, "Intrinsic Noise of Semiconductor Lasers in Optical Communication Systems," *Opt. Quantum Electron.* 12,207 (1980).
25. N. Chinone, T. Kuroda, T. Ohtoshi, T. Takahashi, and T. Kajimura, "Mode-Hopping Noise in Index-Guided Semiconductor Lasers and Its Reduction by Saturable Absorbers," *IEEE J. Quantum Electron.* QE-21, 1264 (1985).
26. M. Ojima, A. Arimoto, N. Chinone, T. Jotoh, and K. Aiki, "Diode Laser Noise at Control Frequencies in Optical Videodisc Players," *Appl. Opt.* 25, 9, May 1, 1986.
27. D. Treves and D. Bloomberg, "Signal Noise and Codes in Optical Memories," *Optical Engineering* 25, 7, 881, (1986).
28. T. Ikegami, "Spectral Broadening and Trailing Effect in Directly Modulated Injection Lasers," *Technical Digest, First European Conference on Optical Communication, London (1975)*, p. 111.
29. K.Y. Lau, C. Harder, and A. Yariv, "Longitudinal Mode Spectrum of Semiconductor Lasers Under High Speed Modulation," *IEEE J. Quantum Electron.* QE-20, 71 (1984).
30. J. Vanderwall and J. Blackburn, "Suppression of Some Artifacts of Modal Noise in Fiber-Optic Systems," *Opt. Lett.* 4, 295. *Soc. Am* 70, 1565 (1980).
31. M. Ojima, K. Aiki, and S. Yonezawa, "Noise Suppression in Semiconductor Laser Pick-Ups for Video Disk Players," *J. Opt. Soc. Am.* 70, 1565 (1980).
32. A. Ohishi, N. Chinone, M. Ojima, and A. Arimoto, "Noise Characteristics of High-Frequency Superposed Laser Diodes for Optical Disc Systems," *Electron. Lett.* 20, 821 (1984).

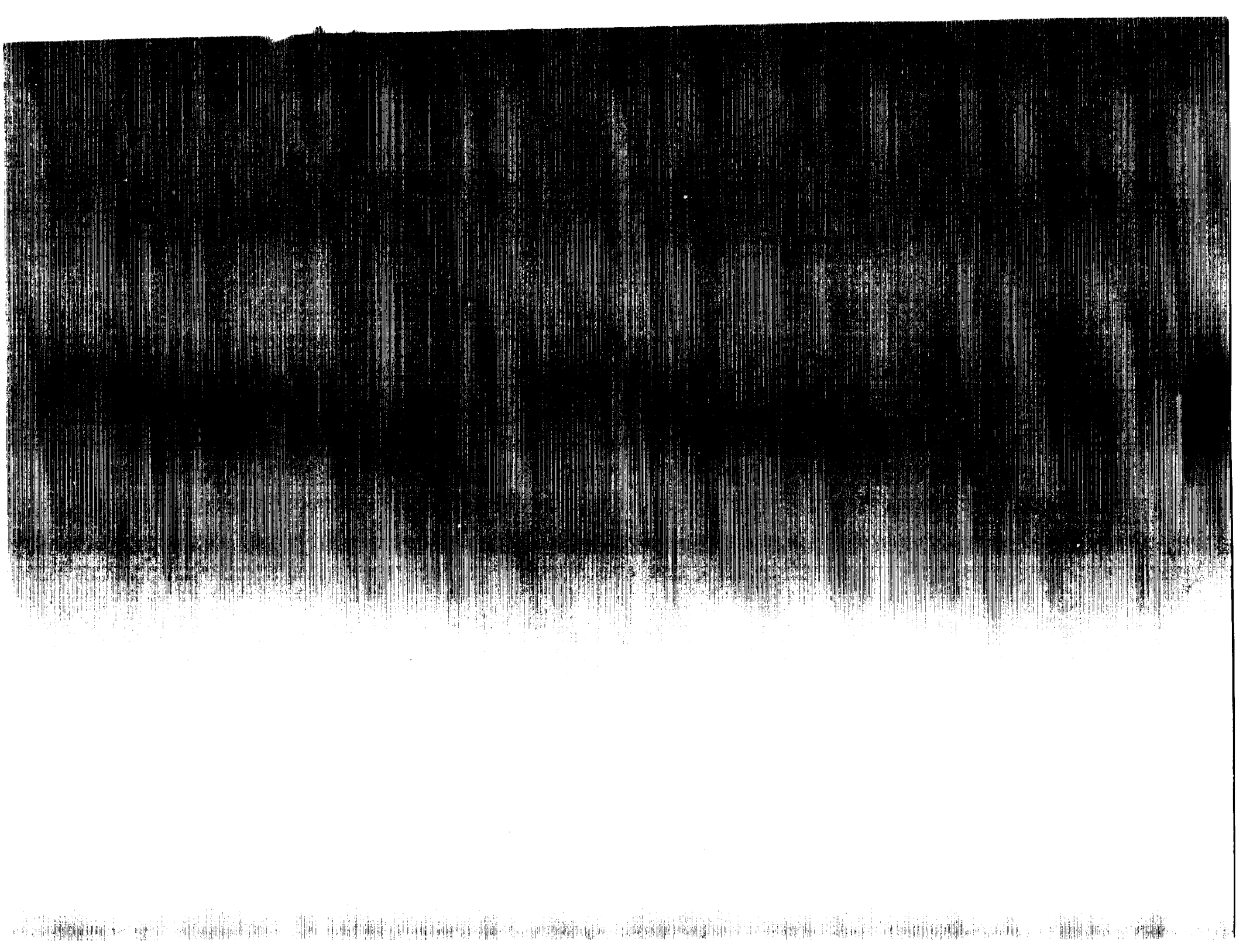
33. A. Arimoto, M. Ojima, N. Chinone, A. Oishi, T. Gotoh, and N. Ohnuki, "Optimum Conditions for the High Frequency Noise Reduction Method in Optical Videodisc Players," *Appl. Opt.* 25, 1398 (1986).
34. Matsui, S., Takiguchi, H., Hayashi, H., Yamamoto, S., Yano, and Hijikata, T.: "Suppression of feedback-induced noise in short-cavity V-channeled substrate inner stripe lasers with self-oscillation," *Appl. Phys. Lett.*, 1983, 43, pp. 210-221.
35. Arimoto, A., Ojima, M., Chinone, N., Oishi, A., Gotoh, T., and Ohnuki, N.: "Optimum conditions for the high frequency noise reduction method in optical videodisc players," *Appl. Opt.*, 1986.
36. Hibiya, T., Ishikawa, T., and Ohta, Y.: "Growth and characterization of 300- μm thick Bi-substituted gadolinium iron garnet films for an optical isolator," *IEEE Trans.*, 1986, MAG-22, pp. 11-13.
37. Ishikawa, T., Masumoto, T., Ono, K., and Shiroki, K.: "Optical absorption of Bi-substituted iron garnet LPE films for 0.8 μm optical isolator," *Advances in Magneto-Optics, Proc. Int. Symp. Magneto-Optics J. Magn. Soc. Japan* 1987, 11, pp. 353-356.
38. R. Katayama, Y. Yamanaka, K. Kubota, I. Ishikawa, "Low Noise 0.78 μm -Band Laser Diode Unit Containing Faraday Rotator," *Electron. Lett.* 24, 8, p. 480-481. (1988).
39. G.A. Alphonse, D.B. Gilbert, M. G. Harvey, M. Ettenberg, "High-Power Superluminescent Diodes," *IEEE J. Quant. Electron.* 24, 12, p. 2454-2547 (1988).
40. A. Dandridge and H.F. Taylor, "Noise and Correlation Effects in GaAlAs Broad-Band Devices," *J. Lightwave Tech.* LT-5, 5, 689, (1987).
41. H. Kogelnik and C.V. Shank, "Coupled-Wave Theory of Distributed Feedback Lasers," *J. Appl. Phys.* 43, 2327 (1972).
42. R.F. Kazarinov, and C.H. Henry, "Second-Order Distributed Feedback lasers with Mode Selection Provided by First-Order Radiation Losses," *IEEE J. Quantum Electron.* QE-21, 144 (1985).





1. Report No. NASA CR-4322		2. Government Accession No.		3. Recipient's Catalog No.	
4. Title and Subtitle Linear Laser Diode Arrays for Improvement in Optical Disk Recording for Space Stations				5. Report Date September 1990	
				6. Performing Organization Code	
7. Author(s) G.A. Alphonse D.B. Carlin J.C. Connolly				8. Performing Organization Report No. CR-90-001	
				10. Work Unit No. 506-44-21-01	
9. Performing Organization Name and Address David Sarnoff Research Center Princeton, New Jersey 08540				11. Contract or Grant No. NAS1-18226	
				13. Type of Report and Period Covered Contractor Report March 1988 - Sept. 1989	
12. Sponsoring Agency Name and Address National Aeronautics and Space Administration Langley Research Center Hampton, Virginia 23665-5225				14. Sponsoring Agency Code	
15. Supplementary Notes Langley Technical Monitor: Herbert D. Hendricks Final Report					
16. Abstract The design and fabrication of individually addressable laser diode arrays for high performance magneto-optic recording systems are presented. Ten diode arrays with 30 mW cw light output, linear light vs current characteristics and single longitudinal mode spectrum have been fabricated using CSP (channel substrate planar) structures. Preliminary results on the inverse CSP structure, whose fabrication is less critically dependent on device parameters than the CSP, are also presented. The impact of systems parameters and requirements, in particular, the effect of feedback on laser design is assessed, and techniques to reduce feedback or minimize its effect on systems performance, including mode-stabilized structures, are evaluated.					
17. Key Words (Suggested by Author(s)) Laser diode array Distributed Feedback Distributed Bragg Reflector			18. Distribution Statement Unclassified - Unlimited Subject Category 36		
19. Security Classif. (of this report) Unclassified		20. Security Classif. (of this page) Unclassified		21. No. of pages 96	22. Price A05





National Aeronautics and
Space Administration
Code: NTF

Washington, D.C.
20546-0001

Special Postmark
Permitted by Postnet (NTP-400)

NASA

POSTNET
Permitted by Postnet (NTP-400)

POSTNET